1

SWR1-independent association of H2A.Z to the LINC complex promotes meiotic chromosome motion

4

5 Sara González-Arranz[1], Jennifer M. Gardner[2], Zulin Yu[2], Neem J. Patel[3]*, Jonna Heldrich[3],

6 Beatriz Santos[1], Jesús A. Carballo[4], Sue L. Jaspersen[2,5], Andreas Hochwagen[3] and Pedro A.

7 San-Segundo[1]**

8

9 [1]Instituto de Biología Funcional y Genómica (IBFG). Consejo Superior de Investigaciones

10 Científicas (CSIC) and University of Salamanca. 37007-Salamanca, Spain

11 [2]Stowers Institute for Medical Research. Kansas City, MO. USA.

12 [3] Department of Biology. New York University. New York, NY. USA.

13 [4]Centro de Investigaciones Biológicas Margarita Salas. Consejo Superior de Investigaciones

14 Científicas (CSIC). 28040-Madrid, Spain

15 [5] Department of Molecular and Integrative Physiology, University of Kansas Medical Center.

16 Kansas City, KS. USA.

17
18 *Current address: Department of Plant & Microbial Biology, University of California Berkeley,
19 CA. USA.
20

21

22

23 **Corresponding author:

24 ORCID: 0000-0002-5616-574X

25 E-mail: pedross@usal.es

26 Phone: +34 923294902

27 Mailing address: Instituto de Biología Funcional y Genómica (IBFG). CSIC-USAL.

28 C/ Zacarías González, 2. 37007-Salamanca, Spain

29

30

31

32

33

34 **Running tittle:** H2A.Z promotes meiotic chromosome movement

35

36   **Keywords**

37

38   Meiosis, chromosome movement, LINC complex, H2A.Z, Mps3, Ndj1, yeast

39

40

41

42

43   **Non-standard abbreviations**

44

45   BiFC: Bimolecular Fluorescence Complementation

46   DIC: Differential Interference Contrast

47   KAc: Potassium Acetate

48   NE: Nuclear Envelope

49   LINC: Linker of the Nucleoskeleton and Cytoskeleton

50   rDNA: Ribosomal DNA

51   SC: Synaptonemal Complex

52   SIM: Structured Illumination Microscopy

53   SPB: Spindle Pole Body

54   VC: C-terminal moiety of the Venus fluorescent protein

55   VN: N-terminal moiety of the Venus fluorescent protein

56   WCE: Whole cell extracts

57

ABSTRACT

The H2A.Z histone variant is deposited into chromatin by the SWR1 complex affecting multiple aspects of meiosis. Here we describe a SWR1-independent localization of H2A.Z at meiotic telomeres and the centrosome. We demonstrate that H2A.Z colocalizes and interacts with Mps3, the SUN component of the LINC complex that spans the nuclear envelope and links meiotic telomeres to the cytoskeleton promoting meiotic chromosome movement. H2A.Z also interacts with the meiosis-specific Ndj1 protein that anchors telomeres to the nuclear periphery via Mps3. Telomeric localization of H2A.Z depends on Ndj1 and the N-terminal domain of Mps3. Although telomeric attachment to the nuclear envelope is maintained in the absence of H2A.Z, the distribution of Mps3 is altered. The velocity of chromosome movement during meiotic prophase I is reduced in the *htz1Δ* mutant lacking H2A.Z, but it is unaffected in *swr1Δ* cells. We reveal that H2A.Z is an additional LINC-associated factor that contributes to promote telomere-driven chromosome motion critical for error-free gametogenesis.

74 **INTRODUCTION**

75

76   Meiosis is a special form of cell division that lies at the heart of gametogenesis in most
77 sexually reproducing organisms. During meiosis, a series of complex DNA and chromosome
78 interactions culminate in the accurate segregation of a haploid complement of chromosomes to
79 the gametes (Duro and Marston, 2015; Hunter, 2015; Keeney et al., 2014; Zickler and Kleckner,
80 2015). Chromatin remodeling events, including histone post-translational modifications and
81 incorporation of histone variants, play important roles in several processes during meiotic
82 development (Brachet et al., 2012; Crichton et al., 2014; Ontoso et al., 2014; Yamada et al.,
83 2018a; Yamada and Ohta, 2013).

84   H2A.Z is a variant of the canonical H2A histone that is incorporated into chromatin by
85 the action of the ATP-dependent SWR1 remodeling complex. SWR1 replaces an H2A-H2B
86 dimer by H2A.Z-H2B at defined nucleosomes, preferentially in the vicinity of promoter regions
87 (Luk et al., 2010; Raisner et al., 2005). H2A.Z participates in a number of fundamental
88 biological processes in vegetative cells including transcription regulation, chromatin silencing,
89 DNA damage response and chromosome segregation (Adkins et al., 2013; Billon and Cote,
90 2013; Morillo-Huesca et al., 2010; Weber and Henikoff, 2014). In addition, although the
91 number of meiotic reports is scarce, the roles of H2A.Z during meiosis are also beginning to be
92 elucidated in some model organisms. In plants and fission yeast, H2A.Z is required for initiation
93 of meiotic recombination, although the precise event influenced by H2A.Z appears to be
94 different in both organisms. In *Arabidopsis thaliana*, H2A.Z has been proposed to regulate
95 meiotic double-stand break (DSB) formation and repair by its association to hotspots and by
96 controlling the expression pattern of recombination genes, whereas in *Schizosaccharomyces*
97 *pombe*, H2A.Z impacts meiotic recombination by modulating chromatin architecture and the
98 binding of DSB-formation proteins to cohesin-rich domains (Choi et al., 2013; Qin et al., 2014;
99 Rosa et al., 2013; Yamada et al., 2018b). H2A.Z is also required for proper meiotic development
100 in *Saccharomyces cerevisiae*. The budding yeast *htz1Δ* mutant (lacking H2A.Z) displays slower
101 kinetics of meiotic progression, reduced spore viability and misregulated meiotic gene
102 expression, but meiotic recombination is not, at least drastically, affected. In addition, the
103 meiotic checkpoint response triggered by the absence of the synaptonemal complex (SC) Zip1
104 protein is altered in the *htz1Δ* mutant (Gonzalez-Arranz et al., 2018). Not surprisingly, many of
105 the meiotic functions mentioned above for H2A.Z rely on its chromatin deposition mediated by
106 the SWR1 complex.

107   Curiously, the physical interaction of H2A.Z with non-chromatin components has been
108 reported in high-throughput analyses in *S. cerevisiae* (Bommi et al., 2019; Uetz et al., 2000; Yu

109 et al., 2008). In particular, H2A.Z interacts with the SUN domain-containing Mps3 protein
110 (Gardner et al., 2011). SUN proteins are one of the main components of the evolutionarily
111 conserved LINC (Linker of the Nucleoskeleton and Cytoskeleton) complex that physically
112 connects the nuclear contents with cytoskeletal filaments. The LINC complex is composed of
113 an ensemble of KASH-SUN proteins. The KASH proteins span the outer nuclear membrane to
114 interact with the cytoskeleton and also interact in the perinuclear space with SUN proteins. The
115 SUN proteins, in turn, are embedded in the inner nuclear membrane and protrude towards the
116 nuclear inside (reviewed by (Chang et al., 2015)). LINC complexes participate in a number of
117 cellular functions, such as nuclear positioning, centrosome dynamics and attachment to the
118 nuclear envelope (NE), and DNA Repair (Fernandez-Alvarez et al., 2016; Friederichs et al.,
119 2011; Lawrence et al., 2016; Lee and Burke, 2018). LINC complexes also play a fundamental
120 role in meiotic chromosome movement in all organisms studied (reviewed by (Burke, 2018;
121 Link and Jantsch, 2019)). In budding yeast, two KASH proteins (Mps2 and Csm4) and one
122 SUN protein (Mps3) have been described. In mitotic cells, Mps2 localizes at the yeast
123 centrosome-equivalent called spindle pole body (SPB) forming a non-canonical LINC complex
124 with Mps3 (Chen et al., 2019). In contrast, the meiotically induced Csm4 protein forms LINC
125 complexes with Mps3 along the NE. A recent report has shown that, during meiotic prophase,
126 Mps2 also interacts with Csm4 at the NE mediating the coupling with the Myo2 microfilament
127 motor associated to the actin cytoskeleton (Lee et al., 2020). During meiotic prophase,
128 telomeres are anchored to the nucleoplasmic N-terminal domain of Mps3 by the mediation of
129 the meiosis-specific Ndj1 protein. Forces generated in the cytoplasm by the actin cytoskeleton
130 are transduced through the Myo2/Csm4-Mps3-Ndj1 axis to promote telomere-led chromosome
131 movement (Figure 1A). Besides facilitating homolog interactions that sustain meiotic
132 recombination and chromosome synapsis, these movements have been also proposed to be
133 important to disengage non-homologous chromosome links (Chua and Roeder, 1997; Conrad
134 et al., 1997; Conrad et al., 2008; Conrad et al., 2007; Kosaka et al., 2008; Koszul et al., 2008;
135 Rao et al., 2011; Trelles-Sticken et al., 2000; Wanat et al., 2008).

136   Recent studies have revealed that the telomere-associated Ndj1 protein also localizes to
137 the SPB during meiotic prophase by interacting with Mps3. Ndj1 protein stability in
138 combination with controlled proteolysis of Mps3 at the SPB half-bridge regulate the separation
139 of duplicated SPBs upon meiosis I entry (Li et al., 2017; Li et al., 2015). These and other
140 observations in different organisms support a connection between telomere and centrosome
141 functions that coordinate NE dynamics and meiotic progression (Fernandez-Alvarez and
142 Cooper, 2017).

143   Although most of the roles of the H2A.Z histone variant have been ascribed to its
144   SWR1-dependent chromatin deposition, here we characterize in detail a SWR1-independent
145   interaction of H2A.Z with LINC-associated components, including Mps3 and Ndj1, during
146   meiotic prophase. We show that H2A.Z colocalizes with the SUN protein Mps3 at telomeres
147   and demonstrate that the Mps3-H2A.Z interaction does not occur in the context of chromatin,
148   but depends on the stable attachment of telomeres to the NE. We demonstrate that H2A.Z is an
149   additional novel factor connected with LINC complexes during meiotic prophase that is
150   required for proper meiotic chromosome movement (Figure 1A). We propose that at least some
151   of the meiotic defects of the *htz1* mutant may stem from faulty processes impacted by LINC
152   function.

153
154

155   **RESULTS**

156

157   **H2A.Z remains at chromosome ends in the absence of SWR1**

158   Our previous cytological studies have shown that H2A.Z extensively decorates meiotic
159   chromatin in wild-type pachytene chromosomes, except in the rDNA region where its presence
160   is markedly reduced (Gonzalez-Arranz et al., 2018). In the *swr1Δ* mutant, the bulk of
161   chromatin-associated H2A.Z is lost (Gonzalez-Arranz et al., 2018), but H2A.Z foci persisted in
162   the absence of the SWR1 complex, as seen in enhanced images (Figure 1B, 1C). Double
163   staining with Zip1 antibodies, as a marker of synapsed chromosomes, showed that these SWR1-
164   independent H2A.Z foci were primarily located at chromosome ends (Figure 1B); 65.4% of
165   *swr1Δ* spread nuclei scored (n=26) displayed H2A.Z at telomeres. Consistent with this
166   telomeric localization, *swr1Δ* live meiotic cells expressing a functional *HTZ1-GFP* fusion
167   occasionally displayed H2A.Z spots concentrated at the nuclear periphery in addition to a
168   diffused pan-nuclear signal (Figure 1D). Curiously, whereas H2A.Z is largely excluded from
169   the rDNA chromatin in wild-type nuclei (88.9%; n=27 nuclei), the *swr1Δ* mutant displayed an
170   accumulation of H2A.Z in the nucleolar area (Figure 1B, arrowhead) (50.0%; n=26 nuclei).
171   Nevertheless, this amorphous H2A.Z mass was mainly found inside the loop defined by the
172   unsynapsed rDNA array characteristic of pachytene chromosomes, but it did not appear to be
173   associated with chromatin. A schematic representation of H2A.Z chromosomal localization at
174   pachytene based on cytological observations, in both wild type and *swr1Δ*, is depicted in Figure
175   1E.

176

6
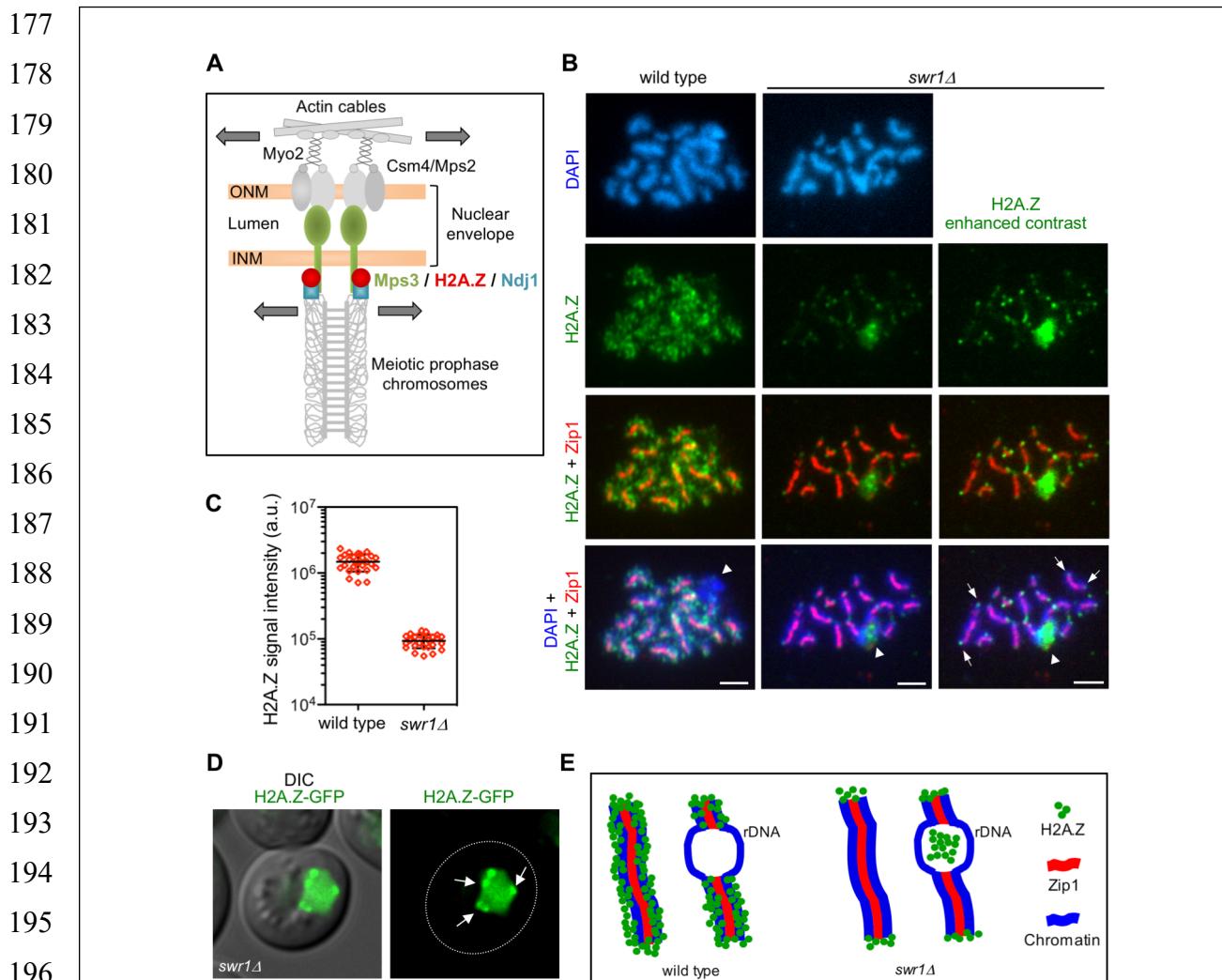
**Figure 1. H2A.Z localizes to chromosome ends during meiotic prophase I.**

(A) Model for LINC-dependent meiotic chromosome movement. Schematic representation of the main components involved in promoting chromosome motion during meiotic prophase I in *Saccharomyces cerevisiae*, including H2A.Z as described here. Colored proteins are the focus of this work. Motion is depicted with arrows. See text for details. ONM: Outer nuclear membrane. INM: Inner nuclear membrane. **(B)** Immunofluorescence of spread pachytene chromosomes from wild type and *swr1Δ* stained with DAPI to visualize chromatin (blue), anti-GFP to detect H2A.Z (green), and anti-Zip1 to mark the SC central region (red). The H2A.Z signal in *swr1Δ* was obtained using a 4-times longer exposure time compared to the wild type. In addition, the contrast of the image shown in the rightmost column was computer-enhanced. Representative nuclei are shown. Spreads were prepared 16 h after meiotic induction. Arrows point to some telomeric H2A.Z foci. Arrowheads mark the nucleolar rDNA region devoid of Zip1. Scale bar, 2 μm. **(C)** Quantification of the total H2A.Z signal in nuclear spreads prepared as in (B). 27 and 26 nuclei from wild type and *swr1Δ*, respectively, were scored. Mean and standard deviation values are represented. **(D)** Representative images from a *swr1Δ* live cell expressing *HTZ1-GFP* 16 h after meiotic induction. Arrows point to H2A.Z foci at the nuclear periphery that stick out over the diffuse pan-nuclear H2A.Z-GFP signal. Scale bar, 2 μm. **(E)** Cartoon representing H2A.Z localization in wild-type and *swr1Δ* pachytene chromosome based on our cytological observations. Strains in (B-C) are: DP840 (*HTZ1-GFP*) and DP841 (*HTZ1-GFP swr1Δ*). Strain in (D) is DP1108 (*HTZ1-GFP swr1Δ*).

Genome-wide association of H2A.Z to meiotic chromatin requires SWR1

Next, we used ChIP-seq to confirm at higher resolution the SWR1 dependency for H2A.Z binding to chromatin during meiotic prophase I. Samples from cultures of wild-type and *swr1Δ* cells expressing *HTZ1-GFP* were processed at zero and 15 hours after meiotic induction. Samples from an untagged control were also taken at the same time points. Profiles of H2A.Z distribution in all chromosomes showed no strong difference between mitotic (t=0h) and meiotic prophase cells (t=15h) and revealed that genome-wide incorporation of H2A.Z is abolished in the absence of SWR1 (Figure S1A-S1C). Consistent with previous reports in mitotic cells showing that H2A.Z is enriched at the nucleosomes flanking the transcription start site of genes (Luk et al., 2010; Raisner et al., 2005), our analysis of H2A.Z position relative to ORFs revealed that, indeed, H2A.Z was enriched at the beginning of ORFs in mitotic cells, thus validating this ChIP-seq study (Figure S1D). We also found the same situation in meiotic cells (Figure S1E). Importantly, the meta-ORF profiles of the *swr1Δ* mutant were similar to those of the untagged control implying that H2A.Z chromatin binding to gene promoters was completely abolished in the absence of SWR1 (Figure S1D, S1E). Thus, like in mitotic cells, the SWR1 complex is absolutely required for genome-wide H2A.Z chromatin deposition also during meiotic prophase I.

H2A.Z interacts and colocalizes with Mps3 at telomeres during meiotic prophase

Previous studies in vegetative cells have described a physical interaction between H2A.Z and the Mps3 protein (Gardner et al., 2011; Morillo-Huesca et al., 2019). Moreover, a recent study also reported co-purification of H2A.Z and Mps3 from meiotic cells using mass spectrometry analysis (Bommi et al., 2019). Consistent with these observations, we found that the H2A.Z-GFP foci detected in some *swr1Δ* live meiotic cells at the nuclear periphery colocalized with Mps3-mCherry (Figure 2A, arrows). Note that there was also a peripheral zone with H2A.Z-GFP, but devoid of Mps3-mCherry (Figure 2A, arrowhead), that corresponds to the accumulation of H2A.Z observed in the vicinity of the nucleolar area in the *swr1Δ* mutant (Figure 1B, 1E; Figure S2; see also Figure 2B). We next used chromosome spreading for a more detailed analysis of H2A.Z and Mps3 colocalization. It has been shown that, despite being embedded in the inner nuclear membrane, the Mps3 protein remains associated to the telomeres in spread preparations of meiotic prophase nuclei (Conrad et al., 2007; Lee et al., 2012). We detected a significant colocalization of H2A.Z and Mps3 foci at telomeres of meiotic prophase chromosomes (Pearson's correlation coefficient 0.741; n=27 nuclei) (Figure 2B), suggesting that H2A.Z and Mps3 also interact during meiotic prophase. To confirm the meiotic interaction between H2A.Z and Mps3 we carried out co-immunoprecipitation experiments. We found that

8

Figure 2. H2A.Z interacts and colocalizes with Mps3 at telomeres.

(A) Images from a representative *swr1Δ* live cell expressing *HTZ1-GFP* and *MPS3-mCherry* 16 h after meiotic induction. Yellow arrows point to areas of the nuclear periphery where H2A.Z and Mps3 display colocalization. The white arrowhead points to the presumed accumulation of H2A.Z at the nucleolus. The differential interference contrast (DIC) image is shown as a reference for the cell outline. Scale bar, 2 μm. **(B)** Immunofluorescence of spread pachytene chromosomes from the *swr1Δ* mutant stained with DAPI to visualize chromatin (blue), anti-GFP to detect H2A.Z (green), and anti-mCherry to detect Mps3 (red). A representative nucleus is shown. The bottom panels display selected individual chromosomes. Spreads were prepared 16 h after meiotic induction. Yellow arrows point to some telomeric foci showing H2A.Z and Mps3 colocalization. The white arrowhead marks the accumulation of H2A.Z at the nucleolar rDNA region in *swr1Δ*. Scale bar, 2 μm. The strains used in (A, B) are DP1108 (*HTZ1-GFP MPS3-mCherry swr1Δ*) and DP1395 (*HTZ1-GFP MPS3-3HA swr1Δ*), respectively. **(C)** Whole cell extracts (WCE) prepared 16 h after meiotic induction were immunoprecipitated using GFP-Trap beads. WCEs and immunoprecipitates (IP) were analyzed by western blot using anti-GFP antibodies (to detect H2A.Z) and anti-HA antibodies (to detect Mps3). Strains used are: DP1394 (*SWR1 HTZ1-GFP MPS3-3HA*), DP1395 (*swr1Δ HTZ1-GFP MPS3-3HA*), DP1330 (*SWR1 HTZ1 MPS3-3HA*) and DP840 (*SWR1 HTZ1-GFP MPS3*). **(D)** WCEs prepared 16 h after meiotic induction were immunoprecipitated using GFP-Trap beads. WCEs and immunoprecipitates (IP) were analyzed by western blot using anti-GFP antibodies (to detect Mps3), and anti-H2A.Z, anti-H2A, anti-H2B, anti-H3 and anti-H4 histone antibodies. Strains used are: DP866 (*SWR1 HTZ1 MPS3-GFP*), DP1102 (*swr1Δ HTZ1 MPS3-GFP*), DP421 (*SWR1 HTZ1 MPS3*) and DP867 (*SWR1 htz1Δ MPS3-GFP*).

Mps3 (tagged with 3HA) was detected in immunoprecipitates of *HTZ1-GFP* strains pulled down with anti-GFP antibodies (Figure 2C). Conversely, H2A.Z was present in immunoprecipitates of *MPS3-GFP* meiotic cells pulled down with anti-GFP antibodies (Figure 2D). Although the amount of H2A.Z was reduced in whole cell extracts (WCE) from the *swr1Δ*

298   mutant, co-immunoprecipitation of H2A.Z and Mps3 occurred both in wild-type and *swr1Δ*

299   meiotic cells (Figure 2C, 2D). Of note, immunoprecipitation of Mps3-GFP specifically brought

300   down H2A.Z, but not the canonical histones (Figure 2D). In sum, these observations indicate

301   that Mps3 and H2A.Z physically interact during meiotic prophase in a SWR1-independent

302   manner. The colocalization at the end of chromosomes suggests that the Mps3-H2A.Z

303   interaction occurs, at least, in the proximity of telomeres.

304

H2A.Z and Ndj1 interact at the nuclear periphery

306   We used the Bimolecular Fluorescence Complementation technique (BiFC) to further

307   explore the physical interaction between H2A.Z and other LINC-associated components, such

308   as Ndj1. BiFC permits direct visualization of protein interaction in living cells based on the

309   association between two nonfluorescent fragments of a fluorescent protein brought in proximity

310   by the interaction between proteins fused to the fragments (Kerppola, 2008; Miller et al., 2015).

311   We found that H2A.Z and Ndj1 interact at the NE, as manifested by the reconstitution of

312   fluorescence from the Venus variant of the Yellow Fluorescent Protein (Venus^{YFP}) at the

313   nuclear periphery in meiotic cells simultaneously expressing both moieties of Venus^{YFP} fused

314   to H2A.Z and Ndj1 (*HTZ1-VN* and *NDJ1-VC*, respectively) (Figure 3A, 3D). Importantly, the

315   H2A.Z-Ndj1 interaction was detected not only in the *swr1Δ* mutant, but also in the wild type

316   (Figure 3B, 3D). This result indicates that the telomeric localization of H2A.Z is not an

317   exclusive feature of the *swr1Δ* mutant, and also occurs in the wild type where it is masked in

318   our cytological analysis of spread nuclei by the massive deposition of H2A.Z throughout the

319   genome. We detected the reconstituted Venus^{YFP} signal in a fraction of cells in the culture

320   (24.2% and 27.3% for wild type and *swr1Δ*, respectively) that roughly represents the population

321   of prophase cells in the asynchronous BR strain background at the time point analyzed. In fact,

322   a parallel meiotic culture used as a control for staging displayed ≈34% cells with Zip1-GFP

323   signal at the same time point. Indeed, the use of a *ndt80Δ* mutation that prevents exit from

324   prophase I increased the proportion of cells displaying H2A.Z-Ndj1 interaction to 54% and

325   55% in *SWR1* and *swr1Δ*, respectively, and the fraction of cells containing the Hop1-GFP

326   prophase I marker to 70% (Figure S3). That is, the interaction was detected in ~80% of prophase

327   cells. This is consistent with the observation that Ndj1-mediated tethering of telomeres to the

328   NE only occurs in meiotic prophase I (Conrad et al., 2007). Of note, when the BiFC assay was

329   performed in cells also expressing *MPS3-mCherry*, we observed that the Venus^{YFP} signal

330   resulting from H2A.Z-Ndj1 interaction largely colocalized with Mps3 foci, thus confirming

331   that it occurs at telomere attachment sites at the NE (Figure 3C; upper row).
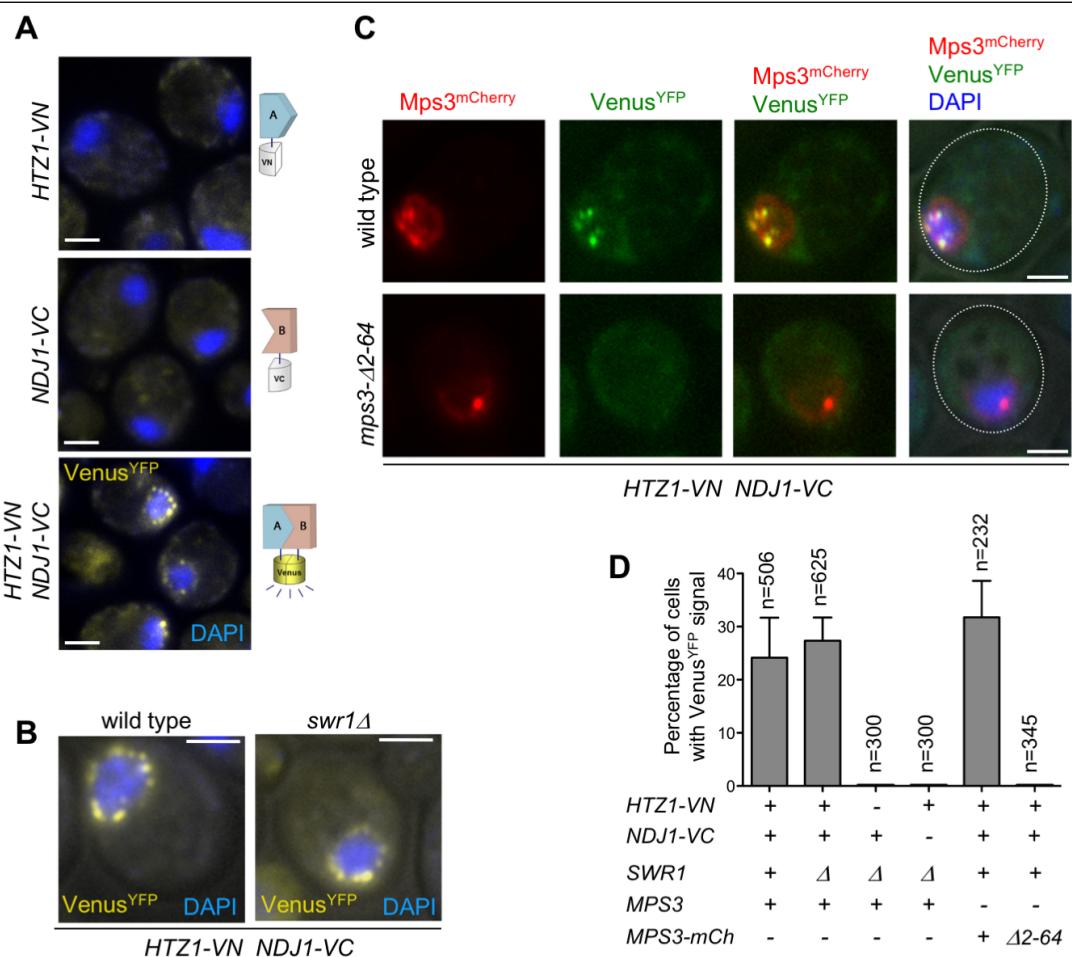
Figure 3. Analysis of H2A.Z and Ndj1 interaction by Bimolecular Fluorescence Complementation (BiFC) assay.

(A-B) H2A.Z and Ndj1 interact at the nuclear periphery. Microscopy fluorescence images of cells expressing *HTZ1* fused to the N-terminal half of the Venus^{YFP} (*VN*) and/or *NDJ1* fused to the C-terminal half of the Venus^{YFP} (*VC*) as indicated. Nuclei are stained with DAPI (blue). The reconstitution of Venus^{YFP} fluorescence resulting from H2A.Z-VN/Ndj1-VC interaction appears in yellow. Images were taken 16 h after meiotic induction. Strains in (A) are: DP1540 (*HTZ1-VN*), DP1541 (*NDJ1-VC*) and DP1493 (*HTZ1-VN NDJ1-VC swr1Δ*). Strains in (B) are DP1496 (*HTZ1-VN NDJ1-VC*) and DP1493 (*HTZ1-VN NDJ1-VC swr1Δ*). **(C)** H2A.Z and Ndj1 interaction at the nuclear periphery depends on the 2-64 N-terminal domain of Mps3. Mps3-mCherry signal is shown in red, Venus^{YFP} in green, and DAPI in blue. Cells were imaged 16 h after meiotic induction. Strains in (C) are: DP1511 (*MPS3-mCherry HTZ1-VN NDJ1-VC*) and DP1512 (*mps3-Δ2-64-mCherry HTZ1-VN NDJ1-VC*). A single medial plane is shown in (A-C). **(D)** Quantification of the percentage of cells displaying Venus^{YFP} fluorescent signal in the experiments shown in (A-C). The analysis was performed in triplicate. The total number of cells scored (n) is shown. Error bars, SD. Scale bar, 2 μm.

Telomeric localization of H2A.Z depends on LINC functional integrity

We next examined H2A.Z localization in mutants that compromise LINC-dependent telomere attachment to the NE, such as *mps3-Δ2-64* and *ndj1Δ*. The *mps3-Δ2-64* mutant lacks the 2-64 amino acids of Mps3 N-terminal domain. In the wild-type Mps3 protein this region protrudes into the nuclear inside serving as telomeric docking site via the Ndj1 protein (Conrad et al., 2007); therefore, in both *mps3-Δ2-64* and *ndj1Δ* mutants, telomere anchoring to the NE is impaired (Figure 4, left panels). We carried out this analysis in a *swr1Δ* mutant to get rid of the massive deposition of H2A.Z throughout chromatin enabling us to detect its telomeric localization. We found that the localization of H2A.Z at telomeres was lost in *swr1Δ mps3-Δ2-64* and *swr1Δ ndj1Δ* spread pachytene nuclei (Figure 4). Moreover, the H2A.Z-Ndj1 interaction detected by BiFC was abolished in the *mps3Δ2-64* mutant (Figure 3C, 3D), further supporting the notion that H2A.Z is recruited to an intact LINC complex. Of note, the presence of H2A.Z in the nucleolar vicinity observed in *swr1Δ* was maintained in the *swr1Δ mps3-Δ2-64* and *swr1Δ ndj1Δ* double mutants (Figure 4, arrowheads). Likewise, a strong H2A.Z focus not associated with the chromosomes that likely corresponds to the SPB (see below) was also detected (Figure 4, yellow arrows). Thus, these observations suggest that the association of H2A.Z to the telomeric regions specifically requires functional anchoring of the chromosomes to the NE mediated by the inner components of LINC.

H2A.Z also colocalizes with Ndj1 and Mps3 at the SPB during meiosis

Several studies have shown that, in addition to telomeres, Mps3 and Ndj1 are also localized at the SPB in meiotic cells (Li et al., 2015; Rao et al., 2011). Since we have observed colocalization and interaction between H2A.Z and Mps3/Ndj1 at telomeres, we examined whether H2A.Z is also targeted to the SPB. In *swr1Δ* live meiotic cells, we observed that one of the peripheral spots of H2A.Z-GFP colocalized with the SPB core component Cnm67-mCherry (Figure 5A). Moreover, BiFC analysis revealed that one of the DAPI-surrounding foci where H2A.Z and Ndj1 interact corresponds to the SPB, as shown by colocalization of the Venus^{YFP} signal with Spc110, another SPB component, tagged with RedStar2 (Figure 5B). Immunofluorescence of spread meiotic chromosomes also showed colocalization between Cnm67 and H2A.Z at a defined focus (Figure 5C). However, in contrast to the telomeric localization of H2A.Z (Figure 4), the presence of H2A.Z at the SPB was maintained in *mps3Δ2-64* and *ndj1Δ* mutants during meiotic prophase, as manifested by the detection of a single H2A.Z focus associated to the characteristic monopolar prophase I spindle stained with tubulin antibodies (Figure S4). Thus, like in telomeres, our results suggest that Mps3, Ndj1 and H2A.Z

400 also interact at the SPB, but our findings reflect differential requirements for targeting H2A.Z
401 to the various subcellular locations.
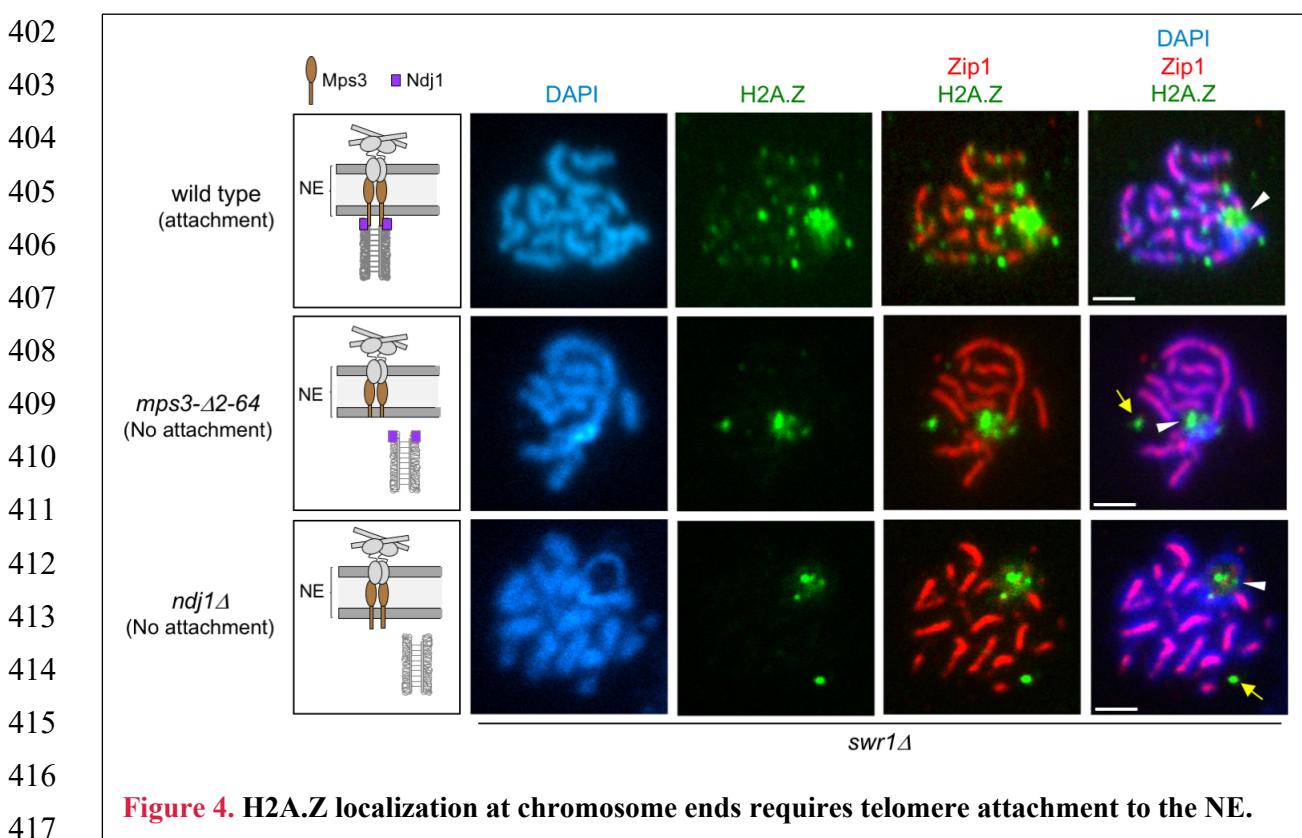
Figure 4. H2A.Z localization at chromosome ends requires telomere attachment to the NE.
Immunofluorescence of spread pachytene nuclei from the *swr1Δ* mutant stained with DAPI to visualize chromatin (blue), anti-GFP to detect H2A.Z (green), and anti-Zip1 to mark the SC central region (red). White arrowheads mark the rDNA region lacking Zip1. Yellow arrows point to H2A.Z foci likely corresponding to the SPB (see text). The cartoons at the left schematize the LINC complex and the status of telomeric attachment in the different situations analyzed. Scale bar, 2 μm. Strains are DP1182 (wild type), DP1280 (*mps3-Δ2-64*) and DP1305 (*ndj1Δ*). 26, 28 and 24 nuclei were examined for wild type, *mps3-Δ2-64* and *ndj1Δ*, respectively.

H2A.Z localizes to the SPB half bridge

425   To determine the precise localization of H2A.Z within the SPB structure during meiotic
426 prophase, we used Structured Illumination Microscopy (SIM). We examined the colocalization
427 of H2A.Z-GFP, as well as Mps3-GFP for comparison, with the Spc110-mCherry protein, a
428 component of the SPB inner plaque (Figure 5D). We focused on prophase cells containing
429 duplicated unseparated SPBs. The old and new SPBs could be distinguished by the stronger
430 and weaker Spc110-mCherry signal, respectively (Burns et al., 2015). Most of the H2A.Z-GFP
431 signal concentrated in the area in between both SPBs that corresponds to the half bridge, and
432 only a limited overlap with the SPBs was observed (Figure 5E, left graph). Like H2A.Z, Mps3-
433 GFP was also detected in the half bridge, but also displayed more extensive colocalization with
434 Spc110-mCherry (Figure 5E, right graph), consistent with the idea that Mps3 is a dual

component of the bridge and the membrane domain that surrounds the SPB core (Chen et al. 2019). Thus, we conclude that the fraction of H2A.Z present in the SPB mainly localizes to the half bridge structure that tethers duplicated SPBs during meiotic prophase I.
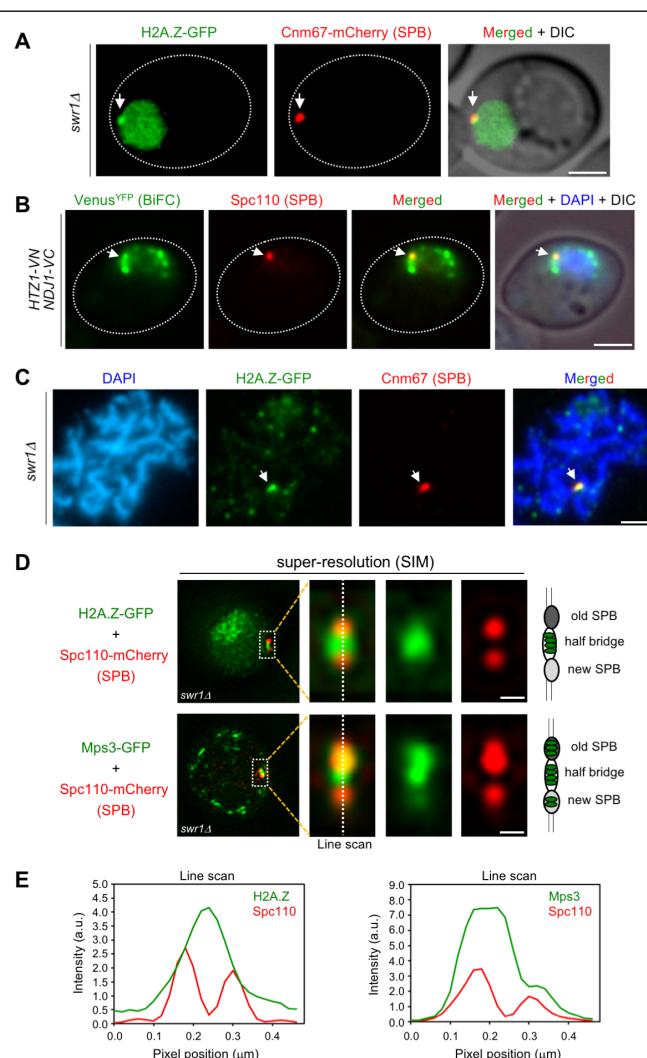

Figure 5. H2A.Z localizes to the SPB half bridge during meiotic prophase I.
(A) Microscopy fluorescence image of a representative *swr1Δ* cell displaying a peripheral concentrated focus (arrow) of H2A.Z-GFP (green) colocalizing with the SPB marker Cnm67-mCherry (red). Images were taken from 16 h meiotic cultures. Scale bar, 2 μm. The strain is DP1172. **(B)** BiFC analysis of Venus^YFP fluorescence (green) reconstituted from H2A.Z-VN/Ndj1-VC interaction in cells also expressing the SPB marker Spc110-RedStar2 (red). Nuclei were stained with DAPI (blue). A representative cell is shown. The arrow points to a single BiFC Venus^YFP focus colocalizing with the SPB. Scale bar, 2 μm. The strain is DP1506. **(C)** Immunofluorescence of a spread pachytene representative nucleus stained with DAPI to visualize chromatin (blue), anti-GFP to detect H2A.Z (green), and anti-mCherry to mark the SPB (red). The arrow points to an H2A.Z focus colocalizing with Cnm67 (SPB). Scale bar, 2 μm. The strain is DP1172. 25 nuclei were examined. **(D)** Structured-Ilumination Microscopy (SIM) fluorescence images of representative *swr1Δ* cells expressing Spc110-mCherry (red) and H2A.Z-GFP (top images) or Mps3-GFP (bottom images), in green. Scale bar, 0.1 μm. **(E)** Average intensity of the indicated proteins along the depicted line scan in all cells analyzed in (D). Strains are DP1578 (*HTZ1-GFP SPC110-mCherry*) and DP1576 (*MPS3-GFP SPC110-mCherry*); 33 and 26 cells were examined, respectively.

Altered distribution of Mps3 along the NE in the absence of H2A.Z

470

471   To further explore the meiotic relationship between Mps3 and H2A.Z, we examined

472   Mps3 levels and localization in the *htz1Δ* mutant. Western blot analysis of Mps3 production in

473   meiotic cultures showed that the protein was heavily induced during meiotic prophase and then

474   declined at late time points as meiosis and sporulation progresses (Figure 6A). The dynamics

475   of Mps3 production was similar in wild type and *htz1Δ*, but global Mps3 levels were reduced

476   in the *htz1Δ* mutant. To rule out the possibility that the reduction in the amount of Mps3 was

477   exclusively due to an inefficient meiotic progression in *htz1Δ* (Gonzalez-Arranz et al., 2018),

478   we measured Mps3 levels in the prophase-arrested *ndt80Δ* mutant, monitoring also Mek1

479   production as a proxy for a meiotic prophase I protein (Ontoso et al., 2013). This analysis

480   revealed that the lack of H2A.Z specifically affects Mps3, but not Mek1, global levels (Figure

481   S5). By immunofluorescence of pachytene chromosome spreads, we found that Mps3 remained

482   at telomeres in the absence of H2A.Z. However, Mps3 telomeric localization was lost in the

483   *ndj1Δ* mutant used as control for comparison (Conrad et al., 2007) (Figure 6B). Thus, although

484   H2A.Z telomeric localization depends on the N-terminal domain of Mps3 (see above), the

485   anchoring of Mps3 to telomeres is independent of H2A.Z. We also examined Mps3-GFP

486   localization in live meiotic cells. The presence of Hop1-mCherry signal was used to stage cells

487   in prophase I (Figure 6C). Analysis of the pattern of Mps3-GFP localization in whole meiotic

488   prophase cells revealed foci with a rather uniform distribution along the NE in the wild type. In

489   contrast, Mps3 showed a more irregular distribution and it appeared to be more concentrated at

490   defined NE regions at a higher frequency in the *htz1Δ* mutant (Figure 6C, 6D; Video S1). We

491   conclude that H2A.Z is required for proper distribution of Mps3 along the NE during meiotic

492   prophase I, but not for telomere attachment.

493

Chromosome motion is reduced in the absence of H2A.Z

494

495   One of the main meiotic functions of the LINC complex is to promote telomere-led

496   chromosome movement during prophase I (Conrad et al., 2008; Koszul et al., 2008). Since we

497   found that H2A.Z interacts with LINC components during meiosis we hypothesized that H2A.Z

498   could also contribute to meiotic chromosome motion. Initially, we used strains expressing

499   *ZIP1-GFP* to follow chromosome movement, as previously described (Scherthan et al., 2007;

500   Sonntag Brown et al., 2011). In addition to wild-type and *htz1Δ* strains, we also analyzed the

501   *ndj1Δ* mutant as a control for defective chromosome mobility and the *swr1Δ* mutant in which

502   H2A.Z is not deposited into the chromatin (see above). To minimize experimental variation,

503   we mixed wild-type and mutant cells from meiotic cultures (16 h) in the same microscopy

15

504 culture chamber to analyze chromosome movement in parallel. Wild-type cells could be easily

505 distinguished by the presence of Pma1-mCherry, a plasma membrane protein that was tagged

506 to mark these cells (Figure 7A). We tracked the ends of individual synapsed chromosomes and

507 measured the distance traveled during a defined time (Figure 7B; Video S2). We found that the

508 average velocity of chromosome movement was reduced in the *htz1Δ* mutant, although to a

509 lesser extent than in *ndj1Δ*. In contrast, the *swr1Δ* mutant was not affected (Figure 7C).
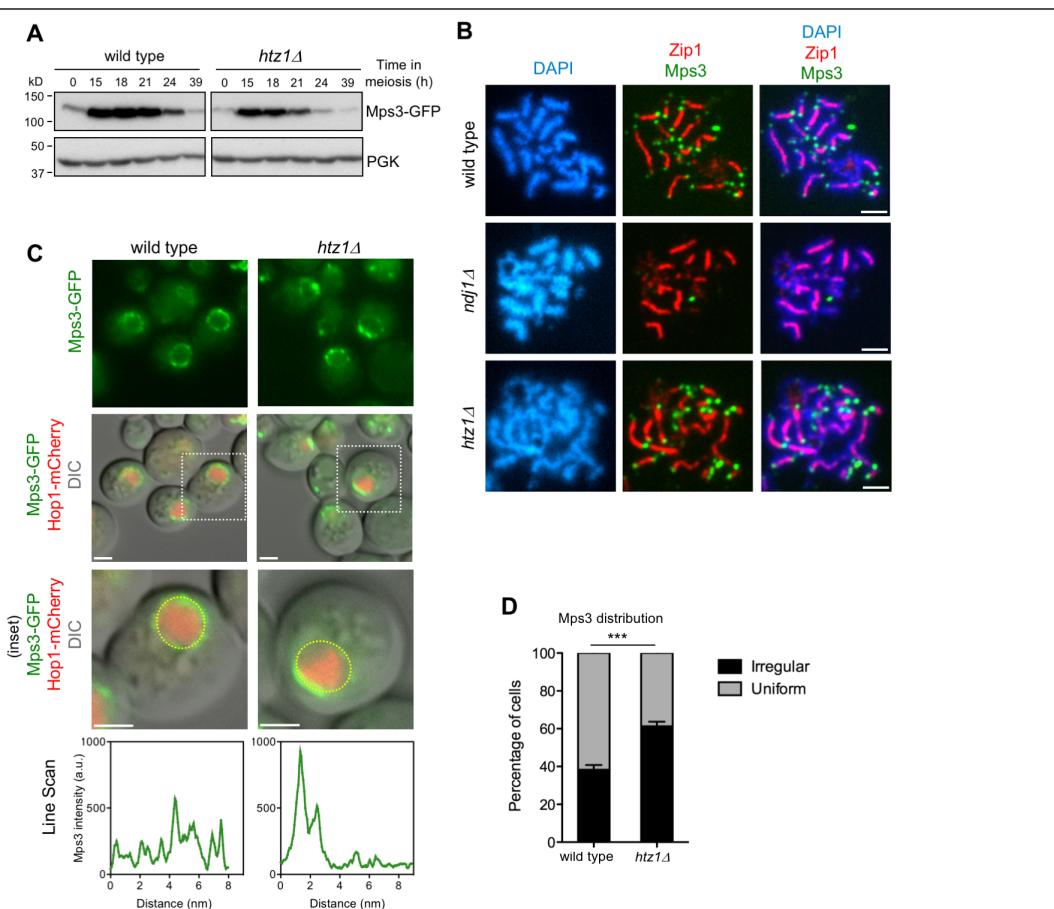
Figure 6. Altered levels and distribution of Mps3 in the absence of H2A.Z.
(A) Western blot analysis of Mps3 production during meiosis detected with anti-GFP antibodies. PGK was used as a loading control. Strains in (A) are: DP866 (wild type) and DP867 (*htz1Δ*). **(B)** Immunofluorescence of spread pachytene nuclei stained with DAPI to visualize chromatin (blue), anti-GFP to detect Mps3 (green), and anti-Zip1 to mark the SC central region (red). Scale bar, 2 μm. Strains in (B) are: DP866 (wild type), DP1103 (*ndj1Δ*) and DP867 (*htz1Δ*). **(C)** Microscopy fluorescence images of cells expressing *MPS3-GFP* and *HOP1-mCherry*. The presence of Hop1-mCherry was used to detect meiotic prophase cells. Stacks of images in the Z-axis were taken, but a single central plane from representative cells is shown. The line scan plots represent the GFP signal along the depicted yellow circle line in the bottom row cells. Scale bar, 2 μm. **(D)** The distribution of Mps3 was analyzed in maximum-intensity projections from images obtained as in (C). Two categories were established: uniform and irregular. Cells scored as "uniform" display Mps3-GFP signal homogeneously distributed. Cells scored as "irregular" display Mps3-GFP signal concentrated to one area of the NE. Only cells displaying Hop1-mCherry signal were considered in the analysis. This quantification was performed in triplicate. A total of 383 and 387 cells were scored for wild type and *htz1Δ*, respectively. Strains in (C-E) are: DP1032 (wild type) and DP1033 (*htz1Δ*).

16

539
540
541
542
543
544
545
546
547
548
549
550
551
552
553
554
555
556
557
558
559
560
561
562
563
564
565
566
567
568
569
570
571
572
573
574
575
576
577
578
579
580
581
582
583
584
585
586
587
588
589
590

Figure 7. H2A.Z drives prophase chromosome movement.
(A) Experimental setup to monitor movement of Zip1-GFP labeled chromosomes. Aliquots of cells from 16-hour meiotic cultures of wild type and *ndj1Δ*, *htz1Δ* or *swr1Δ*, mutants were mixed in microscopy chambers and followed in parallel by time-lapse fluorescence microscopy. Wild-type cells were distinguished by the presence of Pma1-mCherry. (B) Representative images of nuclei from the indicated strains at different time intervals. Zip1-GFP signal is shown. The red line represents the path traveled by an individual chromosome end throughout the time lapse. Scale bar, 1 μm. (C) Quantification of the average velocity of chromosome movement. Mean and SD are represented. Strains are DP1057 (wild type), DP957 (*ndj1Δ*), DP838 (*htz1Δ*) and DP1091 (*swr1Δ*). 25, 16, 18 and 33 chromosome measurements from different cells of wild type, *ndj1Δ*, *htz1Δ* and *swr1Δ*, respectively, were performed in three independent time-lapse experiments.

17

591

592   Velocity measurements based on Zip1-GFP rely on the ability to track a single

593   chromosome pair in the maze of all synapsed chromosomes, which is not always possible.

594   Therefore, for a more extensive and accurate analysis of telomere-driven movement we used a

595   *tetO-tetR* system (Clemente-Blanco et al., 2011) to generate strains harboring the left telomere

596   of chromosome IV (*TEL4L*) labeled with GFP (Figure 8A). These strains also expressed *ZIP1-*

597   *mCherry* as a marker for prophase I stage and synapsed chromosomes (Figure 8B, 8C). In

598   addition, we also introduced the P_{CUP1}-*IME1* construct to increase the synchrony of the meiotic

599   cultures (Chia and van Werven, 2016). *TEL4L* trajectory was tracked in time-lapse experiments

600   of wild-type, *ndj1Δ*, *htz1Δ* and *swr1Δ* strains (Figure 8D; Video S3). Measurement of both

601   average and maximum velocity of *TEL4L* movement during prophase I using this system also

602   revealed that chromosome motion was significantly reduced in the *htz1Δ* mutant (Figure 8E,

603   8F; Figure S6). Interestingly, consistent with the chromatin-independent interaction between

604   H2A.Z and the LINC complex, the *swr1Δ* mutant did not display reduced mobility. As

605   expected, the *ndj1Δ* mutant showed a dramatic reduction in *TEL4L* movement (Figure 8E, 8F;

606   Figure S6). We conclude that H2A.Z is a novel LINC-associated component required for proper

607   chromosome motion during meiotic prophase I.

608

609   **DISCUSSION**

610

611   The H2A.Z histone variant is involved in a myriad of biological processes, both in

612   mitotic and meiotic cells, that rely on its chromatin incorporation at particular genomic

613   positions where the ATP-dependent chromatin remodeler SWR1 is responsible for replacing

614   H2A-H2B dimers to H2A.Z-H2B at nucleosomes (Billon and Cote, 2013). In this work, we

615   characterize in detail an alternative localization of H2A.Z in different sub-compartments of

616   meiotic cells that is independent of SWR1 and, hence, of chromatin. Indeed, our cytological

617   studies of H2A.Z in the *swr1Δ* mutant allowed us to uncover additional locations of H2A.Z

618   (chromosome ends and SPB) that are otherwise masked in wild-type cells due to the widespread

619   incorporation of H2A.Z throughout chromatin. Like in mitotic cells (Raisner et al., 2005), ChIP-

620   seq analysis of H2A.Z distribution during meiotic prophase has confirmed the absence of

621   H2A.Z chromatin deposition throughout the genome during meiosis in the *swr1Δ* mutant; in

622   particular, at gene promoter regions. Here, we describe chromosome movement as a novel

623   SWR1-independent meiotic function for this histone variant.

624

Figure 8. H2A.Z, but not SWR1, is required for proper telomere motion during meiotic prophase.

(A) Schematic representation of GFP tagging of the left telomere of chromosome IV (*TEL4L*). **(B)** Representative image of a live prophase cell expressing *ZIP1-mCherry* (red) with *TEL4L* (arrow) labeled with GFP (green). Scale bar, 2 μm. **(C)** Representative image of a spread pachytene nucleus stained with anti-Zip1 (red), anti-GFP (*TEL4L*; green) and DAPI (blue). Arrow points to *TEL4L*. Scale bar, 2 μm. **(D)** Representative time-lapse fluorescence images of *TEL4L-GFP* at different time intervals (expressed in seconds at the top panels). The red line depicts the path traveled by *TEL4L-GFP* throughout the time lapse. A merge image of DIC, Zip1-mCherry (red) and *TEL4L-GFP* (green) is shown after the last frame. Scale bar, 2 μm. **(E)** Quantification of average velocity of *TEL4L* movement. **(F)** Quantification of maximum velocity of *TEL4L* movement. In (E) and (F), the mean values from three independent experiments are plotted in the graphs. Data from each individual experiment and all multiple statistical comparisons are presented in Figure S6. A total of 101, 146, 172 and 139 measurements of *TEL4L* velocity from wild type, *ndj1Δ*, *htz1Δ* and *swr1Δ*, respectively, were performed in the three independent time-lapse experiments. Strains used in (D-F) are DP1692 (wild type), DP1722 (*ndj1Δ*), DP1693 (*htz1Δ*) and DP1694 (*swr1Δ*).

660   Prompted by our cytological analysis of H2A.Z in the *swr1Δ* mutant during meiotic

661 prophase revealing a telomeric localization and by an earlier report describing the interaction

662 between H2A.Z and Mps3 in vegetative cells (Gardner et al., 2011), we explored the

663 relationship of H2A.Z with LINC components and LINC-associated components, such as the

664 SUN-domain protein Mps3 and the meiosis-specific telomeric protein Ndj1, respectively. The

665 colocalization of H2A.Z with Mps3 at meiotic telomeres and the physical interaction between

666 H2A.Z and both Mps3 and Ndj1, particularly at the NE, strongly suggests that H2A.Z is an

667 additional LINC-associated factor (Figure 1A). It has been proposed that H2A.Z may contribute

668 to the nuclear trafficking of Mps3 in mitotic cells (Gardner et al., 2011); however, we found

669 that Mps3 is still detectable at chromosome ends in the *htz1Δ* mutant, indicating that Mps3 does

670 not require H2A.Z to be delivered to the NE in meiotic cells. Since Mps3 is embedded in the

671 NE, its detection on nuclear spread preparations depends on the attachment of the N-terminal

672 domain to the telomeres via Ndj1 (Conrad et al., 2007). The fact that Mps3 telomeric

673 localization is maintained in the *htz1Δ* mutant also indicates that telomere attachment is not

674 disrupted in the absence of H2A.Z. Nevertheless, we found that the distribution of Mps3

675 throughout the NE is altered in the *htz1Δ* mutant that often displays an aberrant confinement of

676 Mps3 towards one side of the nucleus. Thus, unlike mitotic cells, Mps3 does not require H2A.Z

677 to reach the NE during meiosis, but H2A.Z is required to sustain homogenous distribution of

678 Mps3 along the NE. This accumulation of Mps3 observed in *htz1Δ* is reminiscent of the

679 transient meiotic bouquet (Trelles-Sticken et al., 1999), suggesting that H2A.Z may facilitate

680 the dispersion of telomeres after the bouquet-like stage. The telomeric colocalization and the

681 physical interaction between H2A.Z and Mps3/Ndj1 strongly suggest that H2A.Z directly

682 impinges on LINC dynamics.

683   We found that disruption of telomere attachment, either by deleting *NDJ1* or eliminating

684 the 2-64 amino acids of the Mps3 N-terminal domain, prevents localization of H2A.Z to

685 chromosome ends. This observation suggests that although H2A.Z is not necessary to anchor

686 the telomeres to the NE, it may reinforce the tethering to support robust chromosome

687 movement. A similar scenario has been described in the *mps3-dCC* mutant lacking a fragment

688 of an internal domain of Mps3 located in the lumen of the NE. Like in *htz1Δ*, telomeric

689 attachment is maintained in *mps3-dCC*, but chromosome movement is mildly affected (Lee et

690 al., 2012). Consistent with this notion, the reduction in chromosome velocity detected in *htz1Δ*

691 is not as dramatic as in the *ndj1Δ* mutant where telomere attachment via Mps3 is lost (Conrad

692 et al., 2007). Incorporation of H2A.Z into nucleosomes produces changes in chromatin rigidity

693 (Gerhold et al., 2015; Neumann et al., 2012); thus, it is formally possible that the reduced

694 mobility of *htz1Δ* chromosomes could stem from altered chromatin compaction preventing

695 proper transmission of the forces generated by the actin cytoskeleton to the chromosomes.

696 However, the *swr1Δ* mutant shows no defect in chromosome movement indicating that

697 chromatin deposition of H2A.Z has little impact on this phenomenon. In fact, the interaction

698 between Mps3 and H2A.Z, and between Ndj1 and H2A.Z, persists in the absence of SWR1

699 both in mitotic (Gardner et al., 2011) and meiotic cells (this work). We hypothesize that the

700 irregular accumulation of Mps3 at certain areas of the NE detected in *htz1Δ* cells may interfere

701 with proper telomere-led movement. The involvement of H2A.Z in chromatin movement has

702 been reported also in mitotic cells where H2A.Z promotes the recruitment of unrepairable DSBs

703 to the NE by Mps3 anchoring (Horigome et al., 2014; Kalocsay et al., 2009). However, this

704 nuclear relocalization relies on SWR1-dependent chromatin deposition of H2A.Z, suggesting

705 that different mechanisms are involved.

706 Certain histone post-translational modifications, such as Set1-mediated H3K4

707 methylation have been shown to be involved in bouquet formation and telomere redistribution

708 throughout the NE (Trelles-Sticken et al., 2005). Like H2A.Z, Set1 is also involved in the

709 regulation of the so-called telomere-position effect (TPE) (Krogan et al., 2002; Martins-Taylor

710 et al., 2011; Meneghini et al., 2003). However, the contribution of Set1 and H2A.Z to meiotic

711 nuclear dynamics likely derives from different mechanisms. First, we show here that, unlike

712 TPE (Kobor et al., 2004; Krogan et al., 2003; Mizuguchi et al., 2004), the interaction of H2A.Z

713 with the LINC complex and its role in promoting chromosome movement does not require its

714 SWR1-dependent chromatin incorporation. Second, the telomere dispersion defect of *set1Δ*

715 mutants appears to be independent of Ndj1 (Trelles-Sticken et al., 2005).

716 In addition to the telomeric localization, we also describe here the presence of H2A.Z

717 in another cellular structure devoid of chromatin, the SPB, in particular, the half bridge where

718 Mps3 is also located. However, the targeting of H2A.Z to the SPB presents different

719 requirements because, unlike its telomeric localization, it does not require Ndj1 or the 2-64

720 amino acids of the Mps3 N-terminal domain. Notably, we detect interaction between H2A.Z

721 and Ndj1 in the wild type (Figure 5B), but not in the *mps3Δ2-64* mutant (Figure 3C) consistent

722 with the observation that Ndj1 requires the N-terminal domain of Mps3 for SPB recruitment

723 (Li et al., 2015). What could be the function of H2A.Z at the SPB? During meiotic prophase I,

724 Ndj1, which is recruited to the SPB by Mps3, protects the cohesion between duplicated SPBs

725 (Li et al., 2015). Phosphorylation of Mps3 at S70 promotes the proteolytic cleavage of the

726 protein enabling irreversible separation of sister SPBs (Li et al., 2017). We speculate that the

727 presence of H2A.Z at the SPB at the same time and location as Mps3 and Ndj1 may be

728   indicative of a role for H2A.Z in SPB dynamics; future experiments will address this question.

729   The fact that Mps3, Ndj1 and, as described here, also H2A.Z, colocalize and interact both at

730   telomeres and SPB is consistent with a number of observations indicating that proper nuclear

731   architecture and LINC-mediated contacts between chromosomes and the NE are important to

732   coordinate interhomolog interactions with subsequent chromosome segregation. In *S. pombe,*

733   multiple lines of evidence support this coordination (Fennell et al., 2015; Fernandez-Alvarez et

734   al., 2016; Katsumata et al., 2016; Tomita and Cooper, 2007).

735   In sum, we describe here a novel role for H2A.Z in telomere-led meiotic chromosome

736   motion that is independent of its deposition on chromatin by SWR1. The budding yeast *htz1Δ*

737   mutant displays various meiotic phenotypes including slower meiotic progression and reduced

738   viability of meiotic products. Interestingly, although the *swr1Δ* mutant also shows meiotic

739   defects, these phenotypes are less severe in *swr1Δ* compared to *htz1Δ*. Indeed, spore viability

740   is 95% in the wild type, 76% in *htz1Δ* and 88% in *swr1Δ* (Gonzalez-Arranz et al., 2018),

741   consistent with the notion that H2A.Z possesses additional meiotic roles unrelated to SWR1,

742   namely chromosome motion. Thus, we propose that, at least in budding yeast, H2A.Z performs

743   both chromatin-dependent and chromatin-independent functions all of them contributing to

744   sustain accurate gametogenesis. Cytological analyses of H2A.Z localization in mice

745   spermatocytes have revealed a dynamic spatiotemporal localization of this histone variant on

746   different euchromatin and heterochromatin domains (sex body) suggestive of a functional

747   impact on mammalian meiosis (Greaves et al., 2006; Ontoso et al., 2014). In the future, it will

748   be interesting to determine whether the chromatin-independent function of H2A.Z is also

749   evolutionarily conserved.

750

751   **MATERIALS AND METHODS**

752

753   **Yeast strains**

754   Yeast strain genotypes are listed in Table S1. All the strains are isogenic to the BR1919

755   background (Rockmill and Roeder, 1990). The *swr1::natMX4, swr1::hphMX4, ndj1::natMX4,*

756   *ndj1::kanMX6, htz1::natMX4, mps3::natMX4 and mps3::hphMX4* gene deletions were made

757   using a PCR-based approach (Goldstein and McCusker, 1999; Longtine et al., 1998). The

758   *htz1::URA3* deletion and the functional *HTZ1-GFP* construct were previously described

759   (Gonzalez-Arranz et al., 2018). The *MPS3-GFP, MPS3-3HA, NET1-RedStar2, SPC110-*

760   *RedStar2, SPC110-mCherry, CNM67-mCherry, HOP1-mCherry* and *PMA1-mCherry* gene

761   tagging constructs were also made by PCR (Janke et al., 2004; Longtine et al., 1998; Sheff and

762   Thorn, 2004). To generate P_{CUP1}-*IME1* strains, the 1760 bp promoter region of *IME1,* including

22

763   the *IRT1* lcRNA (Chia and van Werven, 2016), was replaced by the *CUP1* promoter amplified

764   from pYM-N1 (Janke et al., 2004). Strains producing a version of Mps3 lacking amino acids

765   2-64 of the N-terminal domain were created as follows. One allele of the essential *MPS3* gene

766   was deleted in a diploid strain. The heterozygous *MPS3/mps3-hphMX4* diploid was transformed

767   with the *URA3*-based pSS326 centromeric plasmid harboring *mps3Δ2-64*. 5-Fluoroorotic acid

768   (FOA)-resistant and hygromycin-resistant spores were selected and further checked for the

769   presence of *mps3Δ2-64* expressed from pSS326 as the only source of this protein in the cells.

770   As a control, the same procedure was followed using the pSS269 plasmid expressing wild-type

771   *MPS3*. The *HTZ1-VN* and *NDJ1-VC* strains used in the Bimolecular Fluorescence

772   Complementation (BiFC) assay were constructed using the plasmids pFA6a-VN-TRP1 and

773   pFA6a-VC-kanMX6 containing the N-terminal (VN) or C-terminal fragment (VC) of the

774   Venus variant of yellow fluorescent protein (Sung and Huh, 2007). Strains carrying Tel4L

775   marked with GFP were generated as follows. First, the *tetR-GFP* construct was integrated at

776   *leu2* by transforming with the *Afl*II-digested pSS329 plasmid. Second, the *tetO(50)* array was

777   inserted into a region close to the left telomere of chromosome IV (Tel4L) by transforming with

778   the pSS330 plasmid cut with *Afl*II. Strains producing *ZIP1* tagged with mCherry at position 700

779   were constructed using the *delitto perfetto* approach (Stuckey and Storici, 2013). Basically, a

780   fragment containing *mCherry* flanked by 60-nt *ZIP1* sequences upstream and downstream of

781   the codon for amino acid 700 was obtained by PCR from plasmid pSS266. This fragment was

782   transformed into a strain carrying the CORE cassette (*URA3-kanMX4*) inserted at the position

783   corresponding to amino acid 700 of the *ZIP1* gene. FOA-resistant and G418-sensitive

784   transformants were obtained and correct clones were selected.

785   All constructs and mutations were verified by PCR analysis and/or DNA sequencing.

786   The sequences of all primers used in strain construction are available upon request. All strains

787   were made by direct transformation of haploid parents or by genetic crosses always in an

788   isogenic background. Diploids were made by mating the corresponding haploid parents and

789   isolation of zygotes by micromanipulation.

790

791   **Plasmids**

792   The plasmids used in this work are listed in Table S2. To generate pSS266, a PCR

793   fragment containing 468 nt of the *MPS3* promoter, the *MPS3-mCherry* C-terminal fusion and

794   the *ADH1* terminator was amplified from genomic DNA of a strain harboring the *MPS3-*

795   *mCherry* construct and blunt-cloned into the pJET2.1 vector (ThermoFisher). A *Bgl*II-*Bgl*II

796   fragment from pSS266 containing *MPS3-mCherry* was then cloned into *Bam*HI of pRS424 to

797   generate pSS267. Then, a 3.5-kb *Xho*I-*Not*I fragment from pSS267 containing *MPS3-mCherry*

23

798 was cloned into the same sites of the centromeric vector pRS316 to generate pSS269. A version

799 of *MPS3-mCherry* lacking the sequences encoding amino acids 2-64 of the N-terminal domain

800 (*mps3Δ2-64*) was made by site-directed mutagenesis of pSS269 using divergent

801 oligonucleotides flanking the region to be deleted to generate plasmid pSS326. The pSS329

802 plasmid contains the *tet* repressor fused to *NLS-GFP* and expressed from the *URA3* promoter

803 (Michaelis et al., 1997). *Eco*RI or *Afl*II digestion of pSS329 targets TetR-GFP at *leu2*. The

804 pSS330 plasmid harbors an approximately 5.4-kb array with 50 tandem repeats of the *tetO*

805 operator inserted between the *HXT15* and *THI13* genes located close to *TEL4L* cloned into

806 *Bam*HI-*Xba*I of pRS406.

807

Meiotic cultures and synchronous sporulation of BR strains

809 To induce meiosis and sporulation, BR strains were grown in 3.5 ml of 2X Synthetic

810 Complete medium (2% glucose, 0.7% yeast nitrogen base without amino acids, 0.05% adenine,

811 and complete supplement mixture from Formedium at twice the particular concentration

812 indicated by the manufacturer) for 20–24 h, then transferred to 2.5 ml of YPDA (1% yeast

813 extract, 2% peptone, 2% glucose, 0.02% adenine) and incubated to saturation for additional 8

814 hr. Cells were harvested, washed with 2% potassium acetate (KAc), resuspended into 2% KAc

815 (10 ml), and incubated at 30ºC with vigorous shaking to induce meiosis. Both YPDA and 2%

816 KAc were supplemented with 20 mM adenine and 10 mM uracil. The culture volumes were

817 scaled up when needed.

818 To increase synchrony in the meiotic cultures for Tel4L-GFP tracking, BR strains

819 containing P_{CUP1}-*IME1* were used. Culture conditions during pre-sporulation were similar as

820 described above, except that YPDA contained 1% glucose. Cells were transferred to 2% KAc

821 and, after 12 h, CuSO$_4$ was added at a final concentration of 50 μM to induce *IME1* expression

822 and drive meiotic entry. Cells were imaged 6 h after *IME1* induction, when approximately 73%

823 of cells in the culture contained linear stretches of Zip1-mCherry.

824

Western blotting and immunoprecipitation

826 Total cell extracts for western blot analysis in Figure 6A and Figure S5 were prepared

827 by TCA precipitation from 5-ml aliquots of sporulation cultures as previously described

828 (Acosta et al., 2011). The antibodies used are listed in Table S3. The ECL, ECL2 or SuperSignal

829 West Femto reagents (ThermoFisher Scientific) were used for detection. The signal was

830 captured on films and/or with a ChemiDoc XRS system (Bio-Rad).

831 For co-immunoprecipitation experiments, cells from 200 ml of meiotic cultures (16 h

832 after meiotic induction) were harvested and washed with extraction buffer (20 mM HEPES-

24

833   NaOH pH 7.5, 300 mM NaCl, 1mM EDTA, 5 mM EGTA, 50 mM NaF, 50 mM β-

834   glycerophosphate, 1mM DTT, 1mM PMSF) containing one tablet of EDTA-free Complete

835   Protease Inhibitors (Roche). The cell pellet was frozen in liquid nitrogen and ground with a

836   freezer mill (6775 Freezer Mill). Ground cell powder was allowed to thaw on ice and then

837   resuspended in 9 ml of lysis buffer (extraction buffer plus 0.5% Triton X-100). After

838   homogenization with a homogenizer (ultra-turrax T10 basic, IKA) for 30 s, lysates were

839   centrifuged at 3000 x g for 10 min at 4ºC, and the resulting supernatant was used for

840   immunoprecipitation saving 100 µl for input analysis. 50 µl of GFP-Trap magnetic agarose

841   (Chromotek) were added to the remaining lysate to immunoprecipitate GFP-tagged proteins.

842   After 3h incubation with rotation at 4ºC, beads were washed five times with extraction buffer

843   and the bound proteins were eluted by boiling in 2X Laemmli buffer. Samples from both input

844   lysates and immunoprecipitates were analyzed by SDS-PAGE followed by western blotting.

845

846   **Chromatin immunoprecipitation and Illumina sequencing**

847   At the 0 and 15 hour time points, 7 mL meiotic cultures (OD$_{600}$ ~6-7) were harvested

848   and fixed for 30 min with 1% formaldehyde. The crosslinking reaction was quenched by the

849   addition of 125mM glycine. Chromatin immunoprecipitation was performed as described

850   (Blitzblau et al., 2012). Samples were immunoprecipitated with 3 µL polyclonal rabbit anti-

851   GFP serum per IP. Library quality was confirmed by Qubit HS assay kit and 2200 TapeStation.

852   51-bp single-end sequencing was accomplished on an Illumina HiSeq 2500 instrument.

853

854   **Processing Illumina data**

855   Sequencing reads were mapped to a high-quality assembly of S288C (Yue et al., 2017)

856   using Bowtie (Langmead et al., 2009). Reads with up to 2 mismatches across all 51bp were

857   considered during mapping, and reads with more than one reportable alignment were mapped

858   to the best position. Reads were also mapped to the SK1 genome with similar results. Reads

859   were extended towards 3' ends to a final length of 200 bp using MACS-2.1.0

860   (https://github.com/taoliu/MACS) (Zhang et al., 2008) All pileups were SPMR-normalized

861   (signal per million reads) and fold-enrichment of the ChIP data over the input data was

862   calculated. The 95% confidence intervals were calculated by bootstrap resampling from the

863   data 1000 times with replacement. Datasets are available at GEO with accession number

864   GSE153003.

865

866   **Fluorescence microscopy**

25

867   Immunofluorescence of chromosome spreads was performed essentially as described
868 (Rockmill, 2009). The antibodies used are listed in Table S3. Images of spreads and fixed whole
869 cells were captured with a Nikon Eclipse 90i fluorescence microscope controlled with
870 MetaMorph software and equipped with a Hamamatsu Orca-AG CCD camera and a PlanApo
871 VC 100x 1.4 NA objective. The following exposure times were used: DAPI (400 msec), Mps3-
872 GFP/Mps3-HA (500 msec), Cnm67-mCherry (200 msec), tubulin (10 msec) and H2A.Z-GFP
873 (500 msec in wild type and 2000 msec in *swr1*).

874   For BiFC analysis, cells were fixed with 3.7% formaldehyde for 10 minutes at 30ºC
875 with 500 rpm shaking. Cells were washed with 1X PBS, permeabilized for 10 minutes with
876 70% ethanol and stained with 1 µg/ml DAPI for 10 minutes. Images were captured with the
877 Nikon Eclipse 90i fluorescence microscope described above, with the following exposure
878 times: DAPI (400 msec), Venus^{YFP} (5000 msec), Mps3-mCherry (1000 msec), Spc110-
879 RedStar2 (1000 msec) and DIC (10 msec).

880   For analysis of Mps3-GFP distribution, cells were fixed with 3.7 % formaldehyde and
881 washed with 1X PBS. Stacks of 30 planes at 0.2 µm intervals were captured for Mps3-GFP
882 (300 msec exposure). Also, a DIC image (25 msec), and single-plane image of Hop1-mCherry
883 (600 msec exposure), to identify meiotic prophase cells, were captured. Maximum intensity
884 projections were generated using Fiji software (https://imagej.net/Fiji). Images were captured
885 with an Olympus IX71 fluorescence microscope equipped with a personal DeltaVision system,
886 a CoolSnap HQ2 (Photometrics) camera, and a 100x UPLSAPO 1.4 NA objective.

887   For colocalization of H2A.Z-GFP (400 msec exposure) and Mps3-MCherry (800 msec),
888 Cnm67-mCherry (1000 msec) or Net1-RedStar2 (1000 msec) in live meiotic cells, z-stacks of
889 25 planes at 0.2 µm intervals were consecutively captured using the DeltaVision microscope
890 described above. Images were deconvolved using the SoftWoRx 5.0 software (Applied
891 Precisions).

892   For super-resolution analysis (SIM) of Mps3-GFP, H2A.Z-GFP and Spc110-mCherry,
893 cells collected 16 h after meiotic induction were fixed for 15 min in 4% paraformaldehyde (Ted
894 Pella) with 100 mM sucrose, and then washed two times in phosphate-buffered saline pH 7.4.
895 Aliquots of cells were placed on cleaned slides covered with coverslips (number 1.5). Multiple
896 color 3D-SIM images were acquired using a GE Healthcare DeltaVision OMX Blaze V3 fitted
897 with an Olympus PlanApo N 100x 1.42 NA oil objective. Stacks of 17 planes at 0.125 µm
898 intervals were captured (100 msec exposure for green and red channels). SIM reconstruction
899 was performed with the Applied Precision SoftWoRx software package (GE Healthcare,
900 Piscataway, NJ) following the Applied Precision protocols. After reconstruction, alignment
901 between differently colored channels was performed based on calibration from alignment slide

902 provided by the manufacturer. All analysis was performed using ImageJ and custom plugins

903 written for ImageJ (created in the microscopy center of The Stowers Institute for Medical

904 Research) at http://research.stowers.org/imagejplugins/index.html).

905

906 **Measurement of chromosome and telomere movement**

907 For analysis of chromosome movement using Zip1-GFP tracking, cells from 16 h

908 meiotic cultures of wild-type and mutants (*ndj1Δ*, *htz1Δ* or *swr1Δ*) were mixed in the same

909 microscopy culture chamber (μ-slide 8 well, Ibidi) previously treated with 0.5 mg/ml of

910 Concanavalin A Type IV (Sigma-Aldrich). The chamber was maintained at 30ºC during the

911 experiment. Zip1-GFP images were taken during 30 sec at 0.6 sec intervals with 100 msec

912 exposure time. To distinguish wild-type cells (expressing *PMA1-mCherry*) from mutants, red

913 channel images were also taken (800msec). Images were deconvolved using the SoftWoRx 5.0

914 software (Applied Precisions). Clearly isolated chromosomes in a nucleus were manually

915 marked at the end and tracked for 50 consecutive frames. Chromosome velocities were

916 calculated using a manual tracking plugin on ImageJ

917 (https://imagej.nih.gov/ij/plugins/track/track.html). A total 16-25 chromosomes for each

918 genotype in 4 independent experiments were analyzed.

919 For analysis of *TEL4L* movement, meiotic prophase cells from synchronous cultures (6

920 h after induction of *IME1* with CuSO$_4$) were placed in Concanavalin A-treated microscopy

921 culture chambers maintained at 30ºC. For *TEL4L-GFP* (200 msec exposure) and Zip1-mCherry

922 (800 msec exposure), Z-stacks of seven planes (0.6 μm step size) were captured at 8 sec

923 intervals during 180 sec. A single plane of DIC was also captured in every frame. To correct

924 for possible small displacements of the microscope stage during the time lapse, GFP images

925 were aligned using DIC images as reference using a script provided by Giovanni Cardone

926 (available upon request). *TEL4L-GFP* dots in the nuclei were manually marked and tracked for

927 23 consecutive frames. Telomere movement velocities were calculated using the MTrackJ

928 plugin of Fiji (https://imagescience.org/meijering/software/mtrackj/). A total of 101-172

929 telomere tracks from 3 different experiments were analyzed for each genotype. Images for both

930 chromosome movement (Zip1-GFP) and telomere movement (*TEL4L-GFP*) were captured

931 with an Olympus IX71 fluorescence microscope equipped with a personal DeltaVision system,

932 a CoolSnap HQ2 (Photometrics) camera, and a 100x UPLSAPO 1.4 NA objective.

933

934 **Statistics**

935 To determine the statistical significance of differences a two-tailed Student *t*-test, for

936 pairwise comparisons, or one-way ANOVA Tukey test, for multiple comparisons, were used.

937 *P*-Values were calculated with the GraphPad Prism 5.0 software. The nature of errors bars in

938 graphical representations and the number of biological replicates is indicated in the

939 corresponding figure legend.

940

941 **ACKNOWLEDGMENTS**

942

957

958 **AUTHOR CONTRIBUTIONS**

959
960 S González-Arranz: Conceptualization, investigation, formal analysis, visualization

961
962 JM Gardner: Investigation

963
964 Z Yu: Formal analysis

965
966 NJ Patel: Investigation, formal analysis

967
968 J Heldrich: Investigation, formal analysis

969
970 B Santos: Supervision, project administration

971
972 JA Carballo: Resources, funding acquisition

973
974 SL Jaspersen: Resources, funding acquisition

975
976 A Hochwagen: Resources, formal analysis, funding acquisition

977

978   PA San-Segundo: Conceptualization, investigation, supervision, funding acquisition,
979   visualization, writing original draft
980
981   All authors revised, commented and approved the manuscript.
982
983
984   **Conflict of interest statement**

985   The authors declare no competing financial interests.

986

REFERENCES

Acosta, I., D. Ontoso, and P.A. San-Segundo. 2011. The budding yeast polo-like kinase Cdc5 regulates the Ndt80 branch of the meiotic recombination checkpoint pathway. *Mol Biol Cell*. 22:3478-3490.

Adkins, N.L., H. Niu, P. Sung, and C.L. Peterson. 2013. Nucleosome dynamics regulates DNA processing. *Nat Struct Mol Biol*. 20:836-842.

Billon, P., and J. Cote. 2013. Precise deposition of histone H2A.Z in chromatin for genome expression and maintenance. *Biochim Biophys Acta*. 1819:290-302.

Blitzblau, H.G., C.S. Chan, A. Hochwagen, and S.P. Bell. 2012. Separation of DNA replication from the assembly of break-competent meiotic chromosomes. *PLoS Genet*. 8:e1002643.

Bommi, J.R., H. Rao, K. Challa, M. Higashide, K. Shinmyozu, J.I. Nakayama, M. Shinohara, and A. Shinohara. 2019. Meiosis-specific cohesin component, Rec8, promotes the localization of Mps3 SUN domain protein on the nuclear envelope. *Genes Cells*. 24:94-106.

Brachet, E., V. Sommermeyer, and V. Borde. 2012. Interplay between modifications of chromatin and meiotic recombination hotspots. *Biol Cell*. 104:51-69.

Burke, B. 2018. LINC complexes as regulators of meiosis. *Curr Opin Cell Biol*. 52:22-29.

Burns, S., J.S. Avena, J.R. Unruh, Z. Yu, S.E. Smith, B.D. Slaughter, M. Winey, and S.L. Jaspersen. 2015. Structured illumination with particle averaging reveals novel roles for yeast centrosome components during duplication. *Elife*. 4:e08586.

Chang, W., H.J. Worman, and G.G. Gundersen. 2015. Accessorizing and anchoring the LINC complex for multifunctionality. *J Cell Biol*. 208:11-22.

Chen, J., J.M. Gardner, Z. Yu, S.E. Smith, S. McKinney, B.D. Slaughter, J.R. Unruh, and S.L. Jaspersen. 2019. Yeast centrosome components form a noncanonical LINC complex at the nuclear envelope insertion site. *J Cell Biol*. 218:1478-1490.

Chia, M., and F.J. van Werven. 2016. Temporal Expression of a Master Regulator Drives Synchronous Sporulation in Budding Yeast. *G3*. 6:3553-3560.

Choi, K., X. Zhao, K.A. Kelly, O. Venn, J.D. Higgins, N.E. Yelina, T.J. Hardcastle, P.A. Ziolkowski, G.P. Copenhaver, F.C. Franklin, G. McVean, and I.R. Henderson. 2013. Arabidopsis meiotic crossover hot spots overlap with H2A.Z nucleosomes at gene promoters. *Nat Genet*. 45:1327-1336.

Chua, P.R., and G.S. Roeder. 1997. Tam1, a telomere-associated meiotic protein, functions in chromosome synapsis and crossover interference. *Genes Dev*. 11:1786-1800.

Clemente-Blanco, A., N. Sen, M. Mayan-Santos, M.P. Sacristan, B. Graham, A. Jarmuz, A. Giess, E. Webb, L. Game, D. Eick, A. Bueno, M. Merkenschlager, and L. Aragon. 2011. Cdc14 phosphatase promotes segregation of telomeres through repression of RNA polymerase II transcription. *Nat Cell Biol*. 13:1450-1456.

Conrad, M.N., A.M. Dominguez, and M.E. Dresser. 1997. Ndj1p, a meiotic telomere protein required for normal chromosome synapsis and segregation in yeast. *Science*. 276:1252-1255.

1026 Conrad, M.N., C.Y. Lee, G. Chao, M. Shinohara, H. Kosaka, A. Shinohara, J.A. Conchello,
1027 and M.E. Dresser. 2008. Rapid telomere movement in meiotic prophase is promoted by NDJ1,
1028 MPS3, and CSM4 and is modulated by recombination. *Cell*. 133:1175-1187.

1029 Conrad, M.N., C.Y. Lee, J.L. Wilkerson, and M.E. Dresser. 2007. MPS3 mediates meiotic
1030 bouquet formation in *Saccharomyces cerevisiae. Proc Natl Acad Sci U S A*. 104:8863-8868.

1031 Crichton, J.H., C.J. Playfoot, and I.R. Adams. 2014. The role of chromatin modifications in
1032 progression through mouse meiotic prophase. *J Genet Genomics*. 41:97-106.

1033 Duro, E., and A.L. Marston. 2015. From equator to pole: splitting chromosomes in mitosis and
1034 meiosis. *Genes Dev*. 29:109-122.

1035 Fennell, A., A. Fernandez-Alvarez, K. Tomita, and J.P. Cooper. 2015. Telomeres and
1036 centromeres have interchangeable roles in promoting meiotic spindle formation. *J Cell Biol*.
1037 208:415-428.

1038 Fernandez-Alvarez, A., C. Bez, E.T. O'Toole, M. Morphew, and J.P. Cooper. 2016. Mitotic
1039 Nuclear Envelope Breakdown and Spindle Nucleation Are Controlled by Interphase Contacts
1040 between Centromeres and the Nuclear Envelope. *Dev Cell*. 39:544-559.

1041 Fernandez-Alvarez, A., and J.P. Cooper. 2017. Chromosomes Orchestrate Their Own
1042 Liberation: Nuclear Envelope Disassembly. *Trends Cell Biol*. 27:255-265.

1043 Friederichs, J.M., S. Ghosh, C.J. Smoyer, S. McCroskey, B.D. Miller, K.J. Weaver, K.M.
1044 Delventhal, J. Unruh, B.D. Slaughter, and S.L. Jaspersen. 2011. The SUN protein Mps3 is
1045 required for spindle pole body insertion into the nuclear membrane and nuclear envelope
1046 homeostasis. *PLoS Genet*. 7:e1002365.

1047 Gardner, J.M., C.J. Smoyer, E.S. Stensrud, R. Alexander, M. Gogol, W. Wiegraebe, and S.L.
1048 Jaspersen. 2011. Targeting of the SUN protein Mps3 to the inner nuclear membrane by the
1049 histone variant H2A.Z. *J Cell Biol*. 193:489-507.

1050 Gerhold, C.B., M.H. Hauer, and S.M. Gasser. 2015. INO80-C and SWR-C: guardians of the
1051 genome. *J Mol Biol*. 427:637-651.

1052 Goldstein, A.L., and J.H. McCusker. 1999. Three new dominant drug resistance cassettes for
1053 gene disruption in *Saccharomyces cerevisiae. Yeast*. 15:1541-1553.

1054 Gonzalez-Arranz, S., S. Cavero, M. Morillo-Huesca, E. Andujar, M. Perez-Alegre, F. Prado,
1055 and P. San-Segundo. 2018. Functional Impact of the H2A.Z Histone Variant During Meiosis
1056 in *Saccharomyces cerevisiae. Genetics*. 209:997-1015.

1057 Greaves, I.K., D. Rangasamy, M. Devoy, J.A. Marshall Graves, and D.J. Tremethick. 2006.
1058 The X and Y chromosomes assemble into H2A.Z-containing facultative heterochromatin
1059 following meiosis. *Mol Cell Biol*. 26:5394-5405.

1060 Horigome, C., Y. Oma, T. Konishi, R. Schmid, I. Marcomini, M.H. Hauer, V. Dion, M. Harata,
1061 and S.M. Gasser. 2014. SWR1 and INO80 chromatin remodelers contribute to DNA double-
1062 strand break perinuclear anchorage site choice. *Mol Cell*. 55:626-639.

1063 Hunter, N. 2015. Meiotic Recombination: The Essence of Heredity. *Cold Spring Harb Perspect*
1064 *Biol*. 7: a016618.

1065 Janke, C., M.M. Magiera, N. Rathfelder, C. Taxis, S. Reber, H. Maekawa, A. Moreno-Borchart,
1066 G. Doenges, E. Schwob, E. Schiebel, and M. Knop. 2004. A versatile toolbox for PCR-based
1067 tagging of yeast genes: new fluorescent proteins, more markers and promoter substitution
1068 cassettes. *Yeast*. 21:947-962.

1069 Kalocsay, M., N.J. Hiller, and S. Jentsch. 2009. Chromosome-wide Rad51 spreading and
1070 SUMO-H2A.Z-dependent chromosome fixation in response to a persistent DNA double-strand
1071 break. *Mol Cell*. 33:335-343.

1072 Katsumata, K., A. Hirayasu, J. Miyoshi, E. Nishi, K. Ichikawa, K. Tateho, A. Wakuda, H.
1073 Matsuhara, and A. Yamamoto. 2016. A Taz1- and Microtubule-Dependent Regulatory
1074 Relationship between Telomere and Centromere Positions in Bouquet Formation Secures
1075 Proper Meiotic Divisions. *PLoS Genet*. 12:e1006304.

1076 Keeney, S., J. Lange, and N. Mohibullah. 2014. Self-organization of meiotic recombination
1077 initiation: general principles and molecular pathways. *Annu Rev Genet*. 48:187-214.

1078 Kerppola, T.K. 2008. Bimolecular fluorescence complementation (BiFC) analysis as a probe
1079 of protein interactions in living cells. *Annu Rev Biophys*. 37:465-487.

1080 Kobor, M.S., S. Venkatasubrahmanyam, M.D. Meneghini, J.W. Gin, J.L. Jennings, A.J. Link,
1081 H.D. Madhani, and J. Rine. 2004. A protein complex containing the conserved Swi2/Snf2-
1082 related ATPase Swr1p deposits histone variant H2A.Z into euchromatin. *PLoS Biol*. 2:E131.

1083 Kosaka, H., M. Shinohara, and A. Shinohara. 2008. Csm4-dependent telomere movement on
1084 nuclear envelope promotes meiotic recombination. *PLoS Genet*. 4:e1000196.

1085 Koszul, R., K.P. Kim, M. Prentiss, N. Kleckner, and S. Kameoka. 2008. Meiotic chromosomes
1086 move by linkage to dynamic actin cables with transduction of force through the nuclear
1087 envelope. *Cell*. 133:1188-1201.

1088 Krogan, N.J., J. Dover, S. Khorrami, J.F. Greenblatt, J. Schneider, M. Johnston, and A.
1089 Shilatifard. 2002. COMPASS, a histone H3 (Lysine 4) methyltransferase required for telomeric
1090 silencing of gene expression. *J Biol Chem*. 277:10753-10755.

1091 Krogan, N.J., M.C. Keogh, N. Datta, C. Sawa, O.W. Ryan, H. Ding, R.A. Haw, J. Pootoolal,
1092 A. Tong, V. Canadien, D.P. Richards, X. Wu, A. Emili, T.R. Hughes, S. Buratowski, and J.F.
1093 Greenblatt. 2003. A Snf2 family ATPase complex required for recruitment of the histone H2A
1094 variant Htz1. *Mol Cell*. 12:1565-1576.

1095 Langmead, B., C. Trapnell, M. Pop, and S.L. Salzberg. 2009. Ultrafast and memory-efficient
1096 alignment of short DNA sequences to the human genome. *Genome Biol*. 10:R25.

1097 Lawrence, K.S., E.C. Tapley, V.E. Cruz, Q. Li, K. Aung, K.C. Hart, T.U. Schwartz, D.A. Starr,
1098 and J. Engebrecht. 2016. LINC complexes promote homologous recombination in part through
1099 inhibition of nonhomologous end joining. *J Cell Biol*. 215:801-821.

1100 Lee, C.Y., C.G. Bisig, M.M. Conrad, Y. Ditamo, L. Previato de Almeida, M.E. Dresser, and
1101 R.J. Pezza. 2020. Extranuclear Structural Components that Mediate Dynamic Chromosome
1102 Movements in Yeast Meiosis. *Curr Biol*. 30:1207-1216.

Lee, C.Y., M.N. Conrad, and M.E. Dresser. 2012. Meiotic chromosome pairing is promoted by telomere-led chromosome movements independent of bouquet formation. *PLoS Genet*. 8:e1002730.

Lee, Y.L., and B. Burke. 2018. LINC complexes and nuclear positioning. *Semin Cell Dev Biol*. 82:67-76.

Li, P., H. Jin, B.A. Koch, R.L. Abblett, X. Han, J.R. Yates, 3rd, and H.G. Yu. 2017. Cleavage of the SUN-domain protein Mps3 at its N-terminus regulates centrosome disjunction in budding yeast meiosis. *PLoS Genet*. 13:e1006830.

Li, P., Y. Shao, H. Jin, and H.G. Yu. 2015. Ndj1, a telomere-associated protein, regulates centrosome separation in budding yeast meiosis. *J Cell Biol*. 209:247-259.

Link, J., and V. Jantsch. 2019. Meiotic chromosomes in motion: a perspective from *Mus musculus* and *Caenorhabditis elegans*. *Chromosoma* 128:317-330.

Longtine, M.S., A. McKenzie, 3rd, D.J. Demarini, N.G. Shah, A. Wach, A. Brachat, P. Philippsen, and J.R. Pringle. 1998. Additional modules for versatile and economical PCR-based gene deletion and modification in *Saccharomyces cerevisiae*. *Yeast*. 14:953-961.

Luk, E., A. Ranjan, P.C. Fitzgerald, G. Mizuguchi, Y. Huang, D. Wei, and C. Wu. 2010. Stepwise histone replacement by SWR1 requires dual activation with histone H2A.Z and canonical nucleosome. *Cell*. 143:725-736.

Martins-Taylor, K., U. Sharma, T. Rozario, and S.G. Holmes. 2011. H2A.Z (Htz1) controls the cell-cycle-dependent establishment of transcriptional silencing at *Saccharomyces cerevisiae* telomeres. *Genetics*. 187:89-104.

Meneghini, M.D., M. Wu, and H.D. Madhani. 2003. Conserved histone variant H2A.Z protects euchromatin from the ectopic spread of silent heterochromatin. *Cell*. 112:725-736.

Michaelis, C., R. Ciosk, and K. Nasmyth. 1997. Cohesins: chromosomal proteins that prevent premature separation of sister chromatids. *Cell*. 91:35-45.

Miller, K.E., Y. Kim, W.K. Huh, and H.O. Park. 2015. Bimolecular Fluorescence Complementation (BiFC) Analysis: Advances and Recent Applications for Genome-Wide Interaction Studies. *J Mol Biol*. 427:2039-2055.

Mizuguchi, G., X. Shen, J. Landry, W.H. Wu, S. Sen, and C. Wu. 2004. ATP-driven exchange of histone H2AZ variant catalyzed by SWR1 chromatin remodeling complex. *Science*. 303:343-348.

Morillo-Huesca, M., M. Clemente-Ruiz, E. Andujar, and F. Prado. 2010. The SWR1 histone replacement complex causes genetic instability and genome-wide transcription misregulation in the absence of H2A.Z. *PLoS One*. 5:e12143.

Morillo-Huesca, M., M. Murillo-Pineda, M. Barrientos-Moreno, E. Gomez-Marin, M. Clemente-Ruiz, and F. Prado. 2019. Actin and Nuclear Envelope Components Influence Ectopic Recombination in the Absence of Swr1. *Genetics*. 213:819-834.

Neumann, F.R., V. Dion, L.R. Gehlen, M. Tsai-Pflugfelder, R. Schmid, A. Taddei, and S.M. Gasser. 2012. Targeted INO80 enhances subnuclear chromatin movement and ectopic homologous recombination. *Genes Dev*. 26:369-383.

1143   Ontoso, D., I. Acosta, F. van Leeuwen, R. Freire, and P.A. San-Segundo. 2013. Dot1-dependent
1144   histone H3K79 methylation promotes activation of the Mek1 meiotic checkpoint effector
1145   kinase by regulating the Hop1 adaptor. *PLoS Genet*. 9:e1003262.

1146   Ontoso, D., L. Kauppi, S. Keeney, and P.A. San-Segundo. 2014. Dynamics of DOT1L
1147   localization and H3K79 methylation during meiotic prophase I in mouse spermatocytes.
1148   *Chromosoma*. 123:147-164.

1149   Qin, Y., L. Zhao, M.I. Skaggs, S. Andreuzza, T. Tsukamoto, A. Panoli, K.N. Wallace, S. Smith,
1150   I. Siddiqi, Z. Yang, R. Yadegari, and R. Palanivelu. 2014. ACTIN-RELATED PROTEIN6
1151   Regulates Female Meiosis by Modulating Meiotic Gene Expression in Arabidopsis. *Plant Cell*.
1152   26:1612-1628.

1153   Raisner, R.M., P.D. Hartley, M.D. Meneghini, M.Z. Bao, C.L. Liu, S.L. Schreiber, O.J. Rando,
1154   and H.D. Madhani. 2005. Histone variant H2A.Z marks the 5' ends of both active and inactive
1155   genes in euchromatin. *Cell*. 123:233-248.

1156   Rao, H.B., M. Shinohara, and A. Shinohara. 2011. Mps3 SUN domain is important for
1157   chromosome motion and juxtaposition of homologous chromosomes during meiosis. *Genes
1158   Cells*. 16:1081-1096.

1159   Rockmill, B. 2009. Chromosome spreading and immunofluorescence methods in
1160   Saccharomyes cerevisiae. *Methods Mol Biol*. 558:3-13.

1161   Rockmill, B., and G.S. Roeder. 1990. Meiosis in asynaptic yeast. *Genetics*. 126:563-574.

1162   Rosa, M., M. Von Harder, R.A. Cigliano, P. Schlogelhofer, and O. Mittelsten Scheid. 2013.
1163   The Arabidopsis SWR1 chromatin-remodeling complex is important for DNA repair, somatic
1164   recombination, and meiosis. *Plant Cell*. 25:1990-2001.

1165   Scherthan, H., H. Wang, C. Adelfalk, E.J. White, C. Cowan, W.Z. Cande, and D.B. Kaback.
1166   2007. Chromosome mobility during meiotic prophase in *Saccharomyces cerevisiae*. *Proc Natl
1167   Acad Sci U S A*. 104:16934-16939.

1168   Sheff, M.A., and K.S. Thorn. 2004. Optimized cassettes for fluorescent protein tagging in
1169   *Saccharomyces cerevisiae*. *Yeast*. 21:661-670.

1170   Sonntag Brown, M., S. Zanders, and E. Alani. 2011. Sustained and rapid chromosome
1171   movements are critical for chromosome pairing and meiotic progression in budding yeast.
1172   *Genetics*. 188:21-32.

1173   Stuckey, S., and F. Storici. 2013. Gene knockouts, in vivo site-directed mutagenesis and other
1174   modifications using the delitto perfetto system in Saccharomyces cerevisiae. *Methods Enzymol*.
1175   533:103-131.

1176   Sung, M.K., and W.K. Huh. 2007. Bimolecular fluorescence complementation analysis system
1177   for in vivo detection of protein-protein interaction in Saccharomyces cerevisiae. *Yeast*. 24:767-
1178   775.

1179   Tomita, K., and J.P. Cooper. 2007. The telomere bouquet controls the meiotic spindle. *Cell*.
1180   130:113-126.

1181   Trelles-Sticken, E., S. Bonfils, J. Sollier, V. Geli, H. Scherthan, and C. de La Roche Saint-
1182   Andre. 2005. Set1- and Clb5-deficiencies disclose the differential regulation of centromere and
1183   telomere dynamics in *Saccharomyces cerevisiae* meiosis. *J Cell Sci*. 118:4985-4994.

1184   Trelles-Sticken, E., M.E. Dresser, and H. Scherthan. 2000. Meiotic telomere protein Ndj1p is
1185   required for meiosis-specific telomere distribution, bouquet formation and efficient homologue
1186   pairing. *J Cell Biol*. 151:95-106.

1187   Trelles-Sticken, E., J. Loidl, and H. Scherthan. 1999. Bouquet formation in budding yeast:
1188   initiation of recombination is not required for meiotic telomere clustering. *J Cell Sci*. 112:651-
1189   658.

1190   Uetz, P., L. Giot, G. Cagney, T.A. Mansfield, R.S. Judson, J.R. Knight, D. Lockshon, V.
1191   Narayan, M. Srinivasan, P. Pochart, A. Qureshi-Emili, Y. Li, B. Godwin, D. Conover, T.
1192   Kalbfleisch, G. Vijayadamodar, M. Yang, M. Johnston, S. Fields, and J.M. Rothberg. 2000. A
1193   comprehensive analysis of protein-protein interactions in *Saccharomyces cerevisiae*. *Nature*.
1194   403:623-627.

1195   Wanat, J.J., K.P. Kim, R. Koszul, S. Zanders, B. Weiner, N. Kleckner, and E. Alani. 2008.
1196   Csm4, in collaboration with Ndj1, mediates telomere-led chromosome dynamics and
1197   recombination during yeast meiosis. *PLoS Genet*. 4:e1000188.

1198   Weber, C.M., and S. Henikoff. 2014. Histone variants: dynamic punctuation in transcription.
1199   *Genes Dev*. 28:672-682.

1200   Yamada, S., K. Kugou, D.Q. Ding, Y. Fujita, Y. Hiraoka, H. Murakami, K. Ohta, and T.
1201   Yamada. 2018a. The conserved histone variant H2A.Z illuminates meiotic recombination
1202   initiation. *Curr Genet*. 64:1015-1019.

1203   Yamada, S., K. Kugou, D.Q. Ding, Y. Fujita, Y. Hiraoka, H. Murakami, K. Ohta, and T.
1204   Yamada. 2018b. The histone variant H2A.Z promotes initiation of meiotic recombination in
1205   fission yeast. *Nucleic Acids Res*. 46:609-620.

1206   Yamada, T., and K. Ohta. 2013. Initiation of meiotic recombination in chromatin structure. *J
1207   Biochem*. 154:107-114.

1208   Yu, H., P. Braun, M.A. Yildirim, I. Lemmens, K. Venkatesan, J. Sahalie, T. Hirozane-
1209   Kishikawa, F. Gebreab, N. Li, N. Simonis, T. Hao, J.F. Rual, A. Dricot, A. Vazquez, R.R.
1210   Murray, C. Simon, L. Tardivo, S. Tam, N. Svrzikapa, C. Fan, A.S. de Smet, A. Motyl, M.E.
1211   Hudson, J. Park, X. Xin, M.E. Cusick, T. Moore, C. Boone, M. Snyder, F.P. Roth, A.L.
1212   Barabasi, J. Tavernier, D.E. Hill, and M. Vidal. 2008. High-quality binary protein interaction
1213   map of the yeast interactome network. *Science*. 322:104-110.

1214   Yue, J.X., J. Li, L. Aigrain, J. Hallin, K. Persson, K. Oliver, A. Bergstrom, P. Coupland, J.
1215   Warringer, M.C. Lagomarsino, G. Fischer, R. Durbin, and G. Liti. 2017. Contrasting
1216   evolutionary genome dynamics between domesticated and wild yeasts. *Nat Genet*. 49:913-924.

1217   Zhang, Y., T. Liu, C.A. Meyer, J. Eeckhoute, D.S. Johnson, B.E. Bernstein, C. Nusbaum, R.M.
1218   Myers, M. Brown, W. Li, and X.S. Liu. 2008. Model-based analysis of ChIP-Seq (MACS).
1219   *Genome Biol*. 9:R137.

1220   Zickler, D., and N. Kleckner. 2015. Recombination, Pairing, and Synapsis of Homologs during
1221   Meiosis. *Cold Spring Harb Perspect Biol*. 7:a016626.
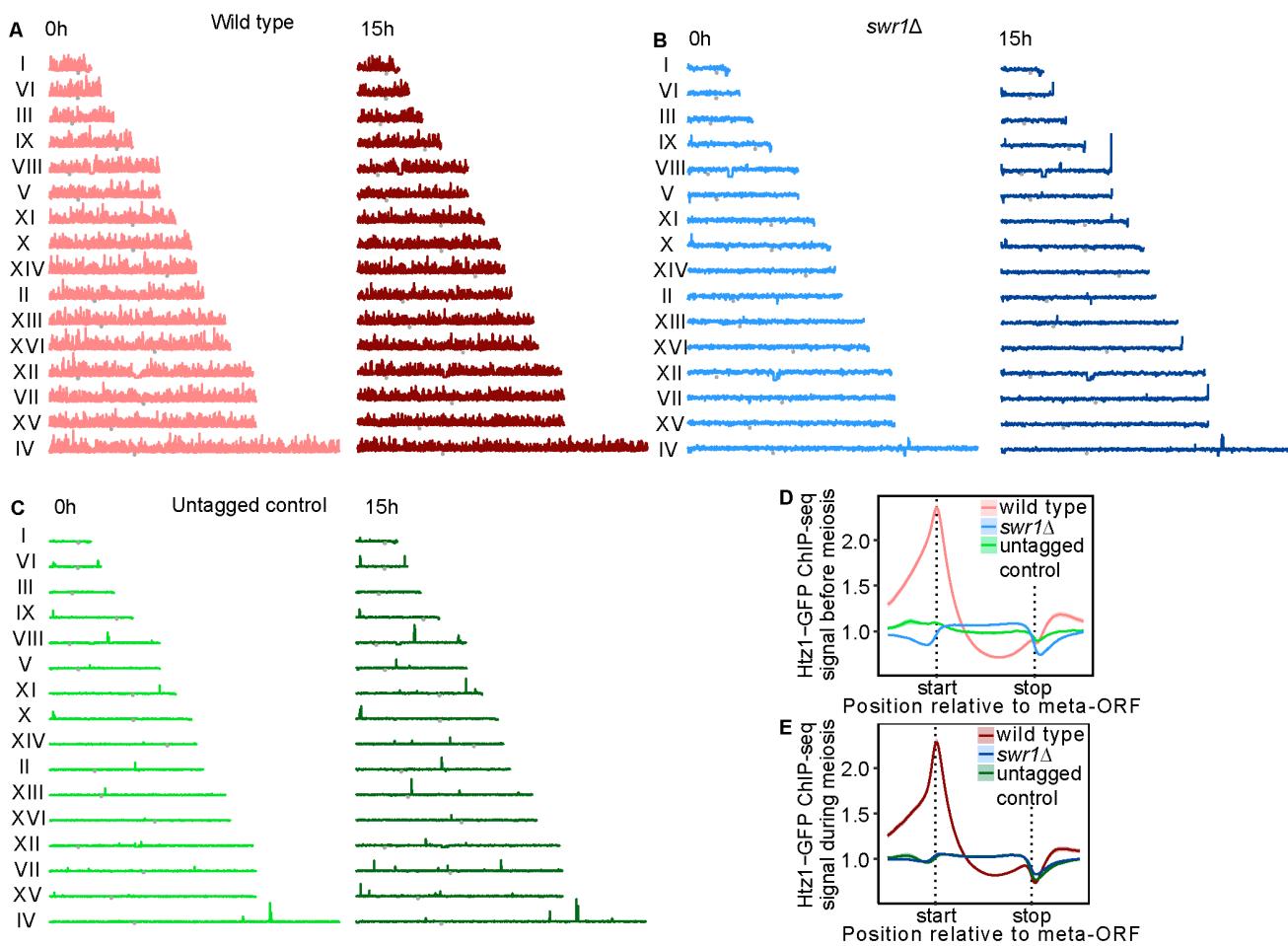
Figure S1. Genome-wide incorporation of H2A.Z to meiotic chromatin depends on SWR1. (Related to Figure 1)

Profiles of H2A.Z binding to all chromosomes in wild type **(A)**, *swr1Δ* **(B)**, and the untagged control **(C)**, determined by ChIP-seq. Gray points indicate the location of the centromere. **(D-E)** Metagene analysis of H2A.Z binding by ChIP-seq. The ORFs are scaled to the "Start" and "Stop" positions, and up- and downstream flanking regions represent half the size of the ORF. Samples were taken at 0 h and 15 h after meiotic induction. Anti-GFP antibodies were used to immunoprecipitate H2A.Z-GFP. Strains are: DP840 (*HTZ1-GFP*), DP841 (*HTZ1-GFP swr1Δ*) and DP421 (*HTZ1* untagged control).

Figure S2. A fraction of H2A.Z accumulates in the vicinity of the nucleolus in *swr1Δ* (Related to Figure 2).

Microscopy fluorescence images of *swr1Δ* cells expressing *HTZ1-GFP* and *NET1-RedStar2* as a nucleolar marker. A single plane of a representative cell displaying a diffuse peripheral accumulation of H2A.Z is shown. The arrowhead points to the nucleolar area marked by Net1. Images were taken 16 h after meiotic induction. Scale bar, 2 μm. The strain is DP1189 (*swr1Δ HTZ1-GFP NET1-RedStar2*).
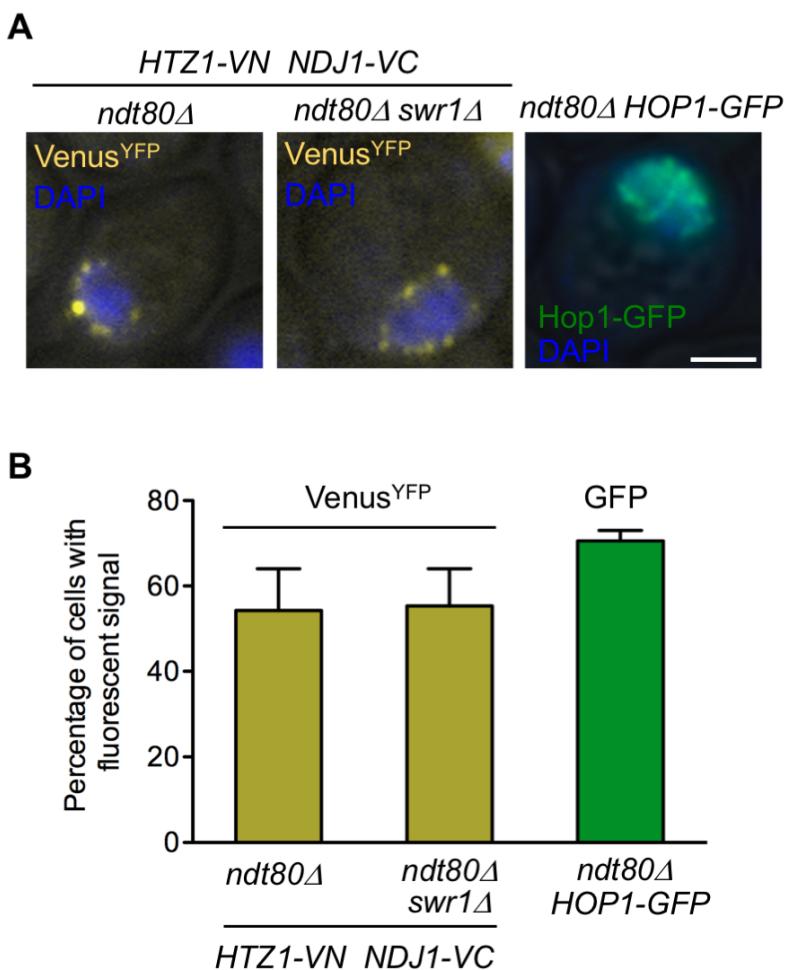
Figure S3. BiFC analysis of H2A.Z-Ndj1 interaction in *ndt80Δ* cells (Related to Figure 3).

(A) Microscopy fluorescence images of *ndt80Δ* and *ndt80Δ swr1Δ* cells expressing *HTZ1* fused to the N-terminal half of the Venus^{YFP} (*VN*) and *NDJ1* fused to the C-terminal half of the Venus^{YFP} (*VC*). Nuclei are stained with DAPI (blue). The reconstitution of Venus^{YFP} fluorescence resulting from H2A.Z-VN/Ndj1-VC interaction appears in yellow. A parallel meiotic culture of *ndt80Δ* cells expressing *HOP1-GFP* (green) was used as control for meiotic prophase I staging. Images were taken 24 h after meiotic induction. Representative cells are shown. Scale bar, 2 μm **(B)** Quantification of the percentage of cells displaying Venus^{YFP} fluorescent signal or Hop1-GFP signal, as indicated. The analysis was performed in triplicate. More than 300 cells were scored in every experiment. Error bars, SD. Strains are: DP1748 (*ndt80Δ HTZ1-VN NDJ1-VC*), DP1749 (*ndt80Δ swr1Δ HTZ1-VN NDJ1-VC*) and DP963 (*ndt80Δ HOP1-GFP*).
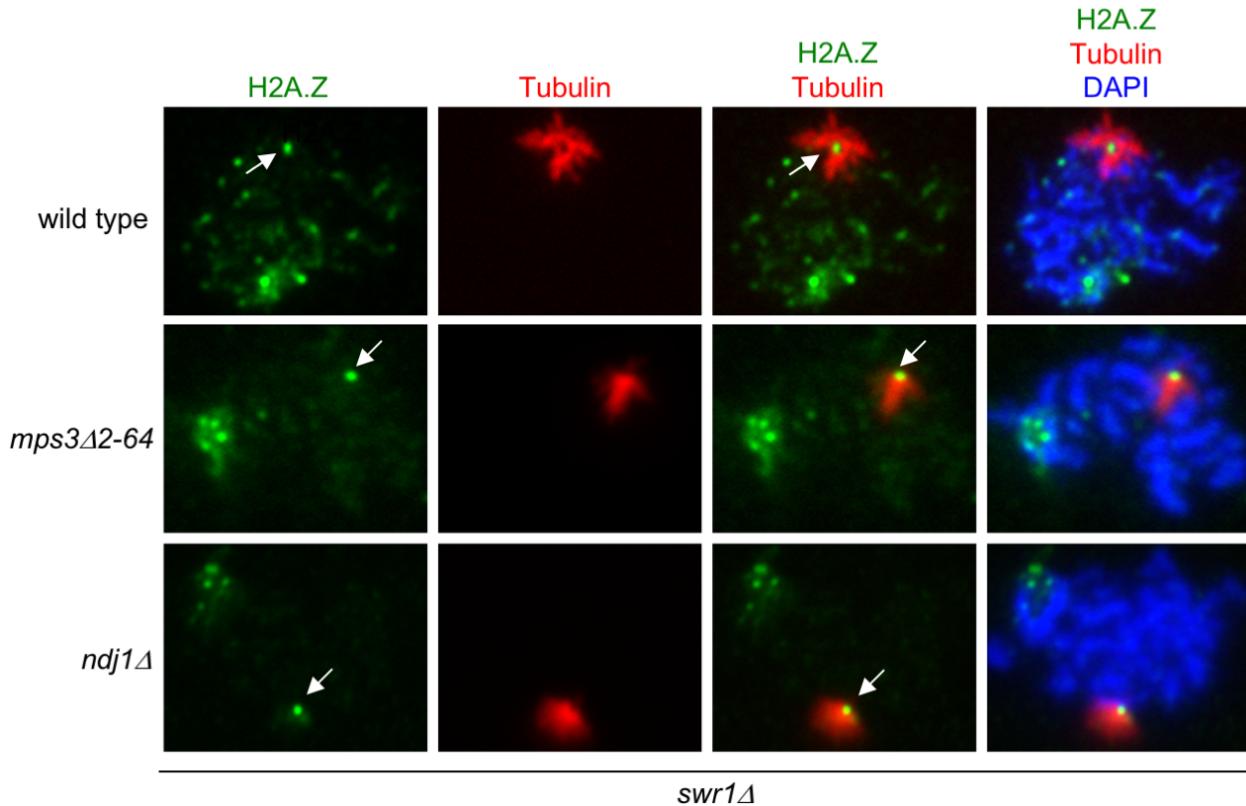
Figure S4. Localization of H2A.Z to the SPB is independent of Ndj1 and the 2-64 N-terminal domain of Mps3. (Related to Figure 5)

Immunofluorescence of representative spread pachytene nuclei stained with DAPI to visualize chromatin (blue), anti-GFP to detect H2A.Z (green), and anti-tubulin to mark the monopolar prophase spindle (red). The arrow points to an H2A.Z focus present at the center of the bushy spindle corresponding to the SPB location. Strains are DP1395 (wild type), DP1280 (*mps3-Δ2-64*) and DP1305 (*ndj1Δ*). 25, 21 and 23 nuclei were examined for wild type, *mps3-Δ2-64* and *ndj1Δ*, respectively.
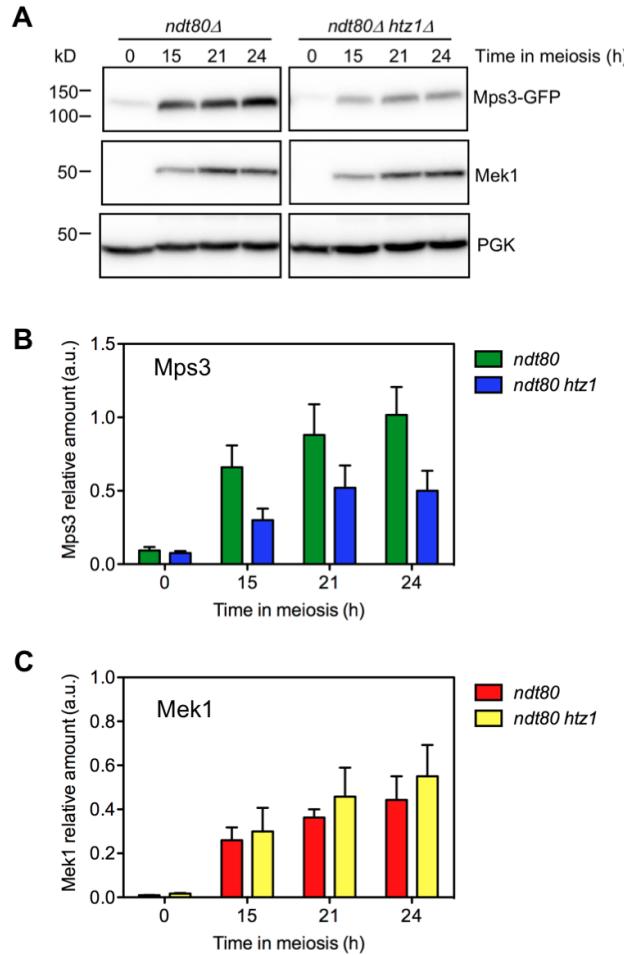
Figure S5. Mps3 global levels are reduced in *ndt80Δ*-arrested cells lacking H2A.Z. (Related to Figure 6)

(A) Western blot analysis of Mps3-GFP and Mek1 production during meiosis detected with anti-GFP and anti-Mek1 antibodies, respectively. PGK was used as a loading control. A representative blot is shown. **(B-C)** Quantification of Mps3-GFP (B) and Mek1 (C) levels normalized to PGK. Average and SEM (error bars) from three independent experiments are shown. Strains are: DP1014 (*ndt80Δ MPS3-GFP*) and DP1013 (*ndt80Δ htz1Δ MPS3-GFP*).

A

Experiment 1

Experiment 2

Experiment 3

B

Average velocity

ANOVA Tukey. Experiment 1

	ndj1Δ	htz1Δ	swr1Δ
wild type	***	***	ns
ndj1Δ		***	***
htz1Δ			**

ANOVA Tukey. Experiment 2

	ndj1Δ	htz1Δ	swr1Δ
wild type	***	**	ns
ndj1Δ		***	***
htz1Δ			***

ANOVA Tukey. Experiment 3

	ndj1Δ	htz1Δ	swr1Δ
wild type	***	***	ns
ndj1Δ		***	***
htz1Δ			*

ANOVA Tukey. 3 experiments

	ndj1Δ	htz1Δ	swr1Δ
wild type	***	***	ns
ndj1Δ		***	***
htz1Δ			**

Maximum velocity

ANOVA Tukey. Experiment 1

	ndj1Δ	htz1Δ	swr1Δ
wild type	***	**	ns
ndj1Δ		***	***
htz1Δ			***

ANOVA Tukey. Experiment 2

	ndj1Δ	htz1Δ	swr1Δ
wild type	***	ns	ns
ndj1Δ		***	***
htz1Δ			**

ANOVA Tukey. Experiment 3

	ndj1Δ	htz1Δ	swr1Δ
wild type	***	***	ns
ndj1Δ		***	***
htz1Δ			*

**ANOVA Tukey. 3 experiments**

	ndj1Δ	htz1Δ	swr1Δ
wild type	***	***	ns
ndj1Δ		***	***
htz1Δ			**

C

		wild type	ndj1Δ	htz1Δ	swr1Δ
Average velocity (µm/s)	Experiment 1	0.086 ± 0.023	0.030 ± 0.011	0.068 ± 0.021	0.082 ± 0.020
	Experiment 2	0.087 ± 0.019	0.03 ± 0.009	0.071 ± 0.023	0.092 ± 0.023
	Experiment 3	0.091 ± 0.021	0.029 ± 0.008	0.074 ± 0.023	0.085 ± 0.019
	Mean 3 experiments	0.088 ± 0.003	0.030 ± 0.001	0.071 ± 0.003	0.086 ± 0.005
Maximum velocity (µm/s)	Experiment 1	0.234 ± 0.062	0.098 ± 0.046	0.185 ± 0.046	0.227 ± 0.064
	Experiment 2	0.223 ± 0.057	0.091 ± 0.030	0.190 ± 0.064	0.238 ± 0.063
	Experiment 3	0.241 ± 0.048	0.089 ± 0.033	0.202 ± 0.054	0.226 ± 0.055
	Mean 3 experiments	0.232 ± 0.009	0.093 ± 0.005	0.192 ± 0.009	0.230 ± 0.007

Figure S6. Analysis of *TEL4L* movement. (Related to Figure 8).
(A) Measurement of average velocity and maximum velocity in three independent time-lapse experiments tracking *TEL4L* movement marked with GFP as depicted in Figure 8. Error bars, SD.
(B) ANOVA statistical analysis of the velocity data obtained in every individual experiment as well as combining the data from all three experiments. **(C)** Mean values for average and maximum velocity. Strains are DP1692 (wild type), DP1722 (*ndj1Δ*), DP1693 (*htz1Δ*) and DP1694 (*swr1Δ*).

Table S1. *Saccharomyces cerevisiae* **strains**

Strain	Genotype	Source
DP421	*MAT**a**/MATα leu2,3-112 his4-260 thr1-4 ura3-1 trp1-289 ade2-1 lys2ΔNheI*	PSS Lab
DP838	DP421 *htz1::URA3 ZIP1-GFP*	This work
DP840	DP421 *HTZ1-GFP::kanMX6*	PSS Lab
DP841	DP421 *swr1::natMX4 HTZ1-GFP::kanMX6*	PSS Lab
DP866	DP421 *MPS3-GFP::kanMX6*	This work
DP867	DP421 *htz1::URA3 MPS3-GFP::kanMX6*	This work
DP957	DP421 *ndj1::natMX4 ZIP1-GFP*	This work
DP963	DP421 *ndt80::LEU2 HOP1-GFP::kanMX6*	PSS Lab
DP1013	DP421 *ndt80:LEU2 htz1::URA3 MPS3-GFP::kanMX6*	This work
DP1014	DP421 *ndt80:LEU2 MPS3-GFP::kanMX6*	This work
DP1032	DP421 *MPS3-GFP::kanMX6 HOP1-mCherry::natMX4*	This work
DP1033	DP421 *htz1::URA3 MPS3-GFP::kanMX6 HOP1-mCherry::natMX4*	This work
DP1057	DP421 *ZIP1-GFP PMA1-mCherry::natMX4*	This work
DP1091	DP421 *swr1::natMX4 ZIP1-GFP*	This work
DP1102	DP421 *swr1::natMX4 MPS3-GFP::kanMX6*	This work
DP1103	DP421 *ndj1::natMX4 MPS3-GFP::kanMX6*	This work
DP1108	DP421 *swr1::natMX4 HTZ1-GFP::kanMX6 MPS3-mCherry::hphMX4*	This work
DP1172	DP421 *HTZ1-GFP::kanMX6 CNM67-mCherry::natMX4 swr1::hphMX4*	This work
DP1182	DP421 *HTZ1-GFP::kanMX6 swr1::hphMX4*	This work
DP1189	DP421 *HTZ1-GFP::kanMX6 NET1-RedStar2::natNT2 swr1::hphMX4*	This work
DP1280	DP421 *mps3::hphMX4 pSS326 [mps3Δ2-64-mCherry URA3] HTZ1-GFP::kanMX6 swr1::natMX4*	This work
DP1305	DP421 *HTZ1-GFP::kanMX6 swr1::natMX4 ndj1::hphMX4*	This work
DP1330	DP421 *MPS3-3HA::kanMX6*	This work

DP1394	DP421 *MPS3-3HA::natMX4 HTZ1-GFP::kanMX6*	This work
DP1395	DP421 *swr1::hphMX4 MPS3-3HA::natMX4 HTZ1-GFP::kanMX6*	This work
DP1493	DP421 *swr1::hphMX4 HTZ1-VN::TRP1 NDJ1-VC::kanMX6*	This work
DP1496	DP421 *HTZ1-VN::TRP1 NDJ1-VC::kanMX6*	This work
DP1506	DP421 *SPC110-RedStar2::natNT2/SPC110 HTZ1-VN::TRP1 NDJ1-VC::kanMX6 swr1::hphMX4*	This work
DP1511	DP421 *mps3::natMX4 pSS269 [MPS3-mCherry URA3] HTZ1-VN::TRP1 NDJ1-VC::kanMX6*	This work
DP1512	DP421 *mps3::natMX4 pSS326 [mps3Δ2-64-mCherry URA3] HTZ1-VN::TRP1 NDJ1-VC::kanMX6*	This work
DP1540	DP421 *HTZ1-VN::TRP1*	This work
DP1541	DP421 *NDJ1-VC::kanMX6*	This work
DP1576	DP421 *MPS3-GFP::kanMX6 swr1::natMX4 SPC110-mCherry::hphNT1/SPC110*	This work
DP1578	DP421 *HTZ1-GFP::kanMX6 swr1::natMX4 SPC110-mCherry::hphNT1/SPC110*	This work
DP1692	DP421 *P_CUP1-IME1::kanMX6 ZIP1-mCherry/ZIP1 TEL4L-tetO(50)::URA3/TEL4L TetR-GFP::LEU2/leu2*	This work
DP1693	DP421 *htz1::natMX4 P_CUP1-IME1::kanMX6 ZIP1-mCherry/ZIP1 TEL4L-tetO(50)::URA3/TEL4L TetR-GFP::LEU2/leu2*	This work
DP1694	DP421 *swr1::hphMX4 P_CUP1-IME1::kanMX6 ZIP1-mCherry/ZIP1 TEL4L-tetO(50)::URA3/TEL4L TetR-GFP::LEU2/leu2*	This work
DP1722	DP421 *ndj1::kanMX6 P_CUP1-IME1::kanMX6 ZIP1-mCherry/ZIP1 TEL4L-tetO(50)::URA3/TEL4L TetR-GFP::LEU2/leu2*	This work
DP1748	DP421 *ndt80::natMX4 HTZ1-VN::TRP1 NDJ1-VC::kanMX6*	This work
DP1749	DP421 *ndt80::natMX4 swr1::hphMX4 HTZ1-VN::TRP1 NDJ1-VC::kanMX6*	This work

*All strains are diploids isogenic to BR1919 (Rockmill and Roeder, 1990). Unless specified, all strains are homozygous for the indicated markers. DP421 is a *lys2* version of the original BR1919-2N.

Rockmill, B., and G.S. Roeder. 1990. Meiosis in asyptic yeast. *Genetics*. 126:563-574.

Table S2. Plasmids

Plasmid	Vector	Relevant parts	Source/Reference
pSS266	pJET2.1	*MPS3-mCherry*	This work
pSS267	pRS424	*2μ TRP1 MPS3-mCherry*	This work
p SS269	pRS316	*CEN6 URA3 MPS3-mCherry*	This work
pSS326	pRS316	*CEN6 URA3 mps3-2-64Δ-mCherry*	This work
pSS329 (pAC32)	unknown	*tetR-NLS-GFP::LEU2*	Andrés Clemente (IBFG)/ (Michaelis et al., 1997)
pSS330 (pAC18)	pRS406	*TEL4L-tetO(50)::URA3*	Andrés Clemente (IBFG)
pFN21	pFA6a	*mCherry::natMX4*	César Roncero (IBFG)

Michaelis, C., R. Ciosk, and K. Nasmyth. 1997. Cohesins: chromosomal proteins that prevent premature separation of sister chromatids. *Cell*. 91:35-45.

Table S3. Primary and secondary antibodies

Antibody	Host and type	Application* (Dilution)	Source / Reference
H2A (acidic patch)	Rabbit polyclonal	WB (1:5000)	Merck 07-146
H2A.Z	Rabbit polyclonal	WB (1:1000)	Active Motif 39647
H2B	Rabbit polyclonal	WB (1:5000)	Abcam ab1790
H3	Rabbit polyclonal	WB (1:5000)	Abcam ab1791
H4	Rabbit polyclonal	WB (1:1000)	Abcam ab10158
Zip1	Rabbit polyclonal	IF (1:300)	S. Roeder
HA (12CA5)	Mouse monoclonal	WB (1:1000)	Roche 11666606001
HA (3F10)	Rat monoclonal	IF (1:225)	Roche 11867431001
GFP (JL-8)	Mouse monoclonal	WB (1:1000-1:2000) IF (1:200)	Clontech 632381
GFP	Rabbit polyclonal	ChIP-seq	R. Freire
mCherry/DsRed	Rabbit polyclonal	IF (1:200)	Clontech 632496
Pgk1 (22C5D8)	Mouse monoclonal	WB (1:5000)	Invitrogen 459250
Mek1	Rabbit polyclonal	WB (1:1000)	Ontoso et al., 2013
Tubulin	Rabbit monoclonal	IF (1:500)	Abcam EPR13798
Anti-mouse-HRP	Sheep polyclonal	WB (1:5000)	GE-Healthcare NA931
Anti-rabbit-HRP	Donkey polyclonal	WB (1:5000)	GE-Healthcare NA934
Anti-mouse AF488	Goat polyclonal	IF (1:200)	Invitrogen A11029
Anti-rabbit AF594	Goat polyclonal	IF (1:200)	Invitrogen A11012
Anti-rat AF568	Goat polyclonal	IF (1:200)	Invitrogen A11077

*WB, western blot; IF, immunofluorescence; ChIP-seq, chromatin immunoprecipitation-sequencing

Ontoso, D., I. Acosta, F. van Leeuwen, R. Freire, and P.A. San-Segundo. 2013. Dot1-dependent histone H3K79 methylation promotes activation of the Mek1 meiotic checkpoint effector kinase by regulating the Hop1 adaptor. *PLoS Genet*. 9:e1003262.